






RESEARCH ARTICLE | DECEMBER 04 2023

# On the behavior of higher harmonics in the evolution of nonlinear water waves in the presence of abrupt depth transitions

Qian Wu (吴倩) ; Xingya Feng (冯兴亚)  ; You Dong ; Frederic Dias *Physics of Fluids* 35, 127102 (2023)<https://doi.org/10.1063/5.0173173>

## Articles You May Be Interested In

Experimental study of extreme waves based on nonlinear Schrödinger equation under background of a random sea

*Physics of Fluids* (April 2023)

Nonlinear Bragg resonance of focused wave groups by periodic seabed topography

*Physics of Fluids* (December 2024)

Partial confinement effects on the performance of a flapping foil power generator

*Physics of Fluids* (February 2023)

**Physics of Fluids**

## Special Topics Open for Submissions

[Learn More](#)

# On the behavior of higher harmonics in the evolution of nonlinear water waves in the presence of abrupt depth transitions

Cite as: Phys. Fluids **35**, 127102 (2023); doi: [10.1063/5.0173173](https://doi.org/10.1063/5.0173173)  
 Submitted: 20 August 2023 · Accepted: 7 November 2023 ·  
 Published Online: 4 December 2023



Qian Wu (吴倩),<sup>1,2</sup> Xingya Feng (冯兴亚),<sup>2,3,a)</sup> You Dong,<sup>1</sup> and Frederic Dias<sup>4</sup>

## AFFILIATIONS

<sup>1</sup>Department of Civil and Environmental Engineering, The Hong Kong Polytechnic University, Hong Kong, China

<sup>2</sup>Department of Ocean Science and Engineering, Southern University of Science and Technology, Shenzhen 518055, China

<sup>3</sup>State Key Laboratory of Coastal and Offshore Engineering, Dalian University of Technology, Dalian, China

<sup>4</sup>School of Mathematics and Statistics, University College Dublin, Dublin D04V1W8, Ireland

<sup>a)</sup>Author to whom correspondence should be addressed: [fengxy@sustech.edu.cn](mailto:fengxy@sustech.edu.cn)

## ABSTRACT

The presence of abrupt depth transitions might trigger strong nonlinear effects on propagating water waves near coastal regions. In this study, the dynamics of nonlinear monochromatic waves over a submerged step representing the abrupt depth transitions are investigated both experimentally and numerically. Within the framework of the free-surface Euler equations, a fully nonlinear potential flow model based on a conformal mapping method is established to investigate the higher harmonics. The numerical method has been well validated with experimental measurements. To analyze the wave nonlinearity at the transitions, the higher harmonics are extracted both in the spatial and time domains. It is shown that abrupt depth transitions enhance the higher harmonic amplitudes in the shallower regions on the step. The effects of the incident wave frequency and height are studied. It is found that the higher harmonics induced by the abrupt depth transitions become more significant with increasing wave steepness. An analysis of the evolution of the skewness and kurtosis demonstrates the high asymmetry of the surface elevation on the upstream junction. The asymmetry shows clear nonlinear effect from the higher harmonics.

Published under an exclusive license by AIP Publishing. <https://doi.org/10.1063/5.0173173>

## I. INTRODUCTION

The occurrence of abnormal large waves can bring significant coastal hazards, especially for the coastal industry and human activities.<sup>1,2</sup> Large extreme waves are more frequently observed and reported in recent years at the background of global climate change.<sup>3,4</sup> Investigation of the underlying mechanism of the formation of large waves has attracted much research interest. Nonlinear wave interaction with suddenly varying bathymetry, i.e., abrupt depth transition (ADT), is believed to be one of the mechanisms to trigger large waves, among many others such as wave focusing, wave-current interaction, modulation instability.<sup>5–10</sup> Accidents have been reported to be caused by large waves at transitional regions of finite to shallow water depths.<sup>3,11,12</sup> This might suggest the role of varying bathymetry, in particular the abrupt depth transitions, in causing extreme wave events where higher harmonics are important.<sup>13–15</sup> To explore the mechanism of large waves triggered by the abrupt depth transitions, it is necessary to investigate the nonlinear effects for wave interactions and the higher harmonic characteristics of wave propagation over the abrupt depth transitions.

Research on wave propagation over a varying bathymetry has been quite active in the last few decades.<sup>16–18</sup> A few studies focus on wave propagation over bathymetry with a simply constant slope.<sup>19–21</sup> Some scholars investigate breakwater performance with different bathymetry shapes in order to explore the most effective one.<sup>22–25</sup> Compared to the work with a constant slope, studies considering sudden depth changes where highly nonlinear waves on the shallow-water region of a submerged step are less reported.<sup>14,26</sup> Massel<sup>27</sup> derived the reflection and transmission coefficients of a long wave traveling over an infinite step. Similarly, Mei *et al.*<sup>28</sup> developed a theory of linear reflection and transmission for both infinite and finite submerged steps. The method was then extended to solve the problem of arbitrary steps with small incident amplitudes.<sup>29</sup> However, a number of recent studies have suggested that a sudden depth transition could play an important role in triggering the occurrence of large waves with consideration of free-surface nonlinear effects.<sup>19,26</sup>

Nonlinear evolution of higher harmonics of waves propagating over the abrupt depth transitions is complex. There could be several

effects induced by the topography, such as refraction, reflection, trapping, and dissipation.<sup>30–34</sup> Massel<sup>27</sup> studied the second harmonics for various finite or infinite submerged steps and analyzed the corresponding reflection coefficients of measurements in a wave tank. The analytical solutions for the second harmonics on a rectangular submerged bar were extended by Li *et al.*<sup>13</sup> and Lee *et al.*<sup>35</sup> Moore *et al.*<sup>36</sup> conducted experiments on the propagation of randomized surface waves. It was found that the theoretical model derived by Majda *et al.*<sup>19</sup> agreed well with the experimental results with the truncated Korteweg–de Vries (TKdV) system. Li *et al.*<sup>13,37</sup> also highlighted the importance of the second nonlinearity considering wavepackets subject to an ADT. However, for studying nonlinear effects the existing studies mostly focus on the second harmonics or the statistical characteristics at the abrupt depth transitions. The characteristics of harmonics higher than the second over a submerged step have not been much studied.<sup>38,39</sup>

In order to study harmonics higher than the second for wave evolution over a varying bathymetry, fully nonlinear potential flow models have been developed in recent years. Galan *et al.*<sup>40</sup> employed a fully nonlinear Boussinesq-type equation to study waves from deep to shallow waters on a submerged trapezoidal step. Zhang and Benoit<sup>15</sup> established a fully nonlinear model by using a spectral approach and studied the irregular waves over the abrupt depth transitions and the statistical results compared well with the experimental results in Trulsen *et al.*<sup>14</sup> Zheng *et al.*<sup>21</sup> carried out fully nonlinear simulations of unidirectional irregular waves on a slope and their numerical results agreed well with the experimental measurements by Trulsen *et al.*<sup>41</sup> To study the strong nonlinear effects resulting from water depth transitions, Viotti *et al.*<sup>42</sup> improved the solutions to the two-dimensional (2D) Euler equations by a conformal mapping method. The conformal mapping method require less effort than direct numerical methods to solve the nonlinear models, such as the KdV and Boussinesq equations.<sup>43</sup> An obvious advantage of the conformal mapping method for investigating nonlinear wave propagation on the abrupt depth transitions is that they eliminate the singularity at the corners of the sudden changes of the sea bottom. In this study, the conformal mapping method is employed to establish a fully nonlinear model for nonlinear wave interactions with varying bathymetry.

The objective of the work is to investigate the importance of higher harmonics of nonlinear water waves propagating on the abrupt depth transitions with efficient numerical simulations and an experimental campaign measurement. Within the framework of potential flow theory, a fully nonlinear model is established to describe the wave evolution on varying bathymetry by a conformal mapping method. Monochromatic waves with varying incident frequencies and steepnesses are studied to examine the changes in the superharmonics on the lee side and on top of the submerged step, especially for the second and third harmonics. We analyze the evolution of wave spectra in both the time and spatial domains to extract the higher harmonics. Two different water depths are employed to study the effects of the water depth ratio of sea bed to the step on the superharmonics. In addition, the nonlinear evolution of wave elevations over the step is discussed in terms of kurtosis and skewness. This provides a more comprehensive and in-depth understanding of wave nonlinearity on the abrupt depth transitions.

The organization of the article is as follows. The experimental setup and the numerical model based on the conformal mapping method are described in Secs. II A and II B, respectively. Convergence

and validation of the numerical model are presented in Sec. II C. The results are discussed in Sec. III. In particular, the dynamic characteristics of the higher harmonics over the abrupt depth transitions are presented in both the time and spatial domains in Secs. III A and III B with both experimental measurements and numerical simulations. Section III C focuses on the distribution of the wave profile parameters in the spatial domain and discusses the effects of water depth on the nonlinear wave evolution. Section IV presents the concluding remarks.

## II. METHODS

### A. Experimental setup

The experiments were conducted in the wave tank located at the Hydraulics Laboratory of the Hong Kong Polytechnic University with a length of 27 m, a width of 0.75 m, and a depth of 1.5 m. A piston-type wavemaker is equipped to generate both monochromatic and irregular waves. At the end of the physical tank, a wave absorber is arranged to dissipate energy, as shown in Fig. 1. The front face of the submerged step was installed 4 m away from the wavemaker providing two depth transitions in the  $x$  axis (same direction as the wave propagation). The water depth on the deeper region is denoted as  $h_1$  and on the shallower region as  $h_2$ . The size of the submerged step is fixed with a length of 2.4 m, a width of 0.75 m and a height of 0.23 m. The value of  $h_2/h_1$  is, thus, adjusted with the water depth  $h_1$ . Eight capacitive wave gauges were used. The origin of the coordinate system is at the center of the step. The positions of WG 1 to WG 8 are listed in Table I. We set  $h_1$  to be 0.36 or 0.48 m. The detailed parameters of the tested cases are shown in Table II. Let  $f_0$  be the incident wave frequency,  $k_1$  the wave number on the deeper region, and  $k_2$  the wave number on the shallower one. Then,  $k_1 a$  denotes the wave steepness where the wave amplitude  $a$  is half the wave height  $a = H/2$ . The cases with  $h_1 = 0.48$  m are denoted with a star (cases 5<sup>a</sup> and 6<sup>a</sup>). A high-resolution camera was placed along the tank to capture the wave profiles. The evolution of monochromatic waves, as depicted in Fig. 2, is examined using a higher frequency of  $f_0 = 1.33$  Hz to clearly illustrate the changes in wave shapes at the shorter wavelength. A comparison with the incident wave profile reveals that the profiles in shallower regions exhibit an asymmetric crest with increased sharpness at the first depth transition. This observation underscores the nonlinear effects in the spatial domain. A comprehensive analysis of the nonlinear characteristics, utilizing both experimental and numerical data, is elaborated upon in Sec. III.

### B. Numerical method

A 2D wave field is described within the framework of potential flow theory and the free-surface Euler system. The fluid is assumed to be inviscid and incompressible, with the flow being irrotational. The flow field can be characterized using a velocity potential  $\phi(x, y, t)$ . For simulation of monochromatic wave propagation over varying bathymetry, a fully nonlinear model based on the conformal mapping method is utilized.<sup>42,44</sup> The governing equation and the boundary conditions read

$$\nabla^2 \phi = 0 \quad b(x) \leq y \leq \eta(x, t), \quad (1)$$

$$\eta_t + \phi_x \eta_x - \phi_y = 0 \quad y = \eta(x, t), \quad (2)$$

$$\phi_t + \frac{1}{2} (\phi_x^2 + \phi_y^2) + g\eta = 0 \quad y = \eta(x, t), \quad (3)$$

$$\phi_y = 0 \quad y = b(x), \quad (4)$$

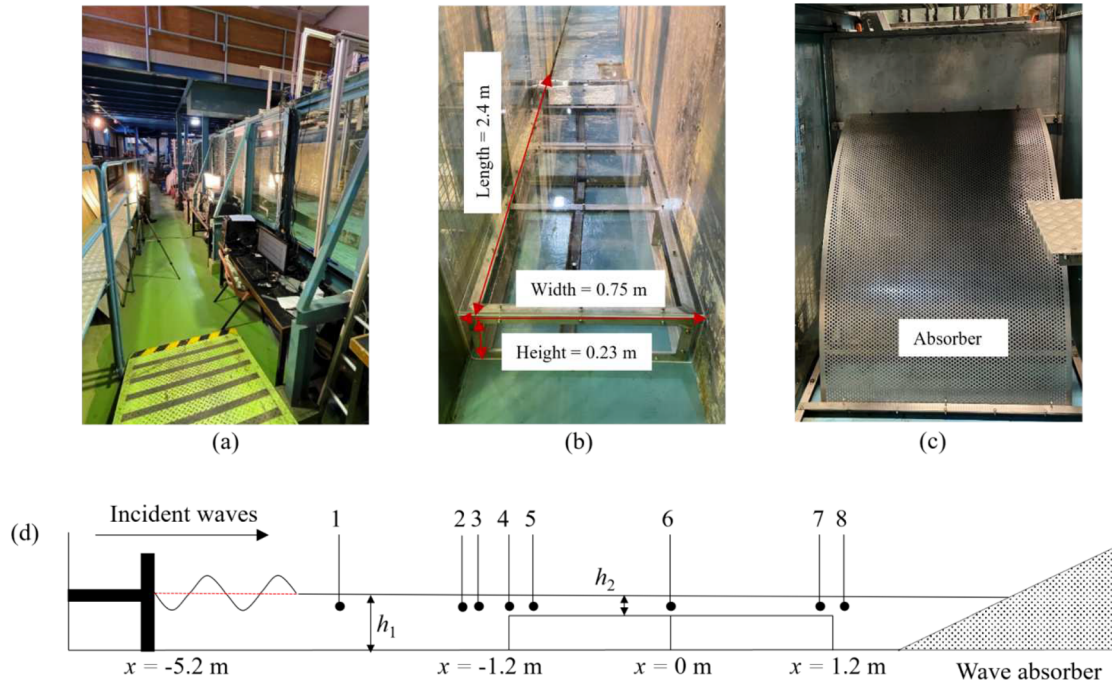


FIG. 1. (a) Laboratory wave tank, (b) stainless rectangular step, (c) wave absorber, and (d) sketch of the experimental setup (not in correct scale for tank length).

TABLE I. Locations of the eight wave gauges shown in Fig. 1.

WG No.	WG 1	WG 2	WG 3	WG 4	WG 5	WG 6	WG 7	WG 8
Position (m)	-2.2	-1.56	-1.4	-1.2	-1.0	0	1.1	1.3

TABLE II. Test parameters. The ratios  $h_2/h_1$  of water depths in shallower region  $h_2$  to that of deeper region  $h_1$  are 0.36 and 0.52, respectively.  $f_0$  is the incident frequency. The wave number  $k_1$  for the monochromatic waves is computed from the dispersion relation using the wave conditions on the deeper region with  $h_1$ .  $a$  is the incident measured wave amplitude.  $k_2$  is derived by the stream function with the incident amplitude  $a$  and shallower region  $h_2$ .

Case	$h_1$ (m)	$h_2/h_1$	$f_0$ (Hz)	$k_1 a$	$k_1 h_1$	$k_2 h_2$
1	0.36	0.36	0.94	0.06	1.434	0.736
2	0.36	0.36	0.94	0.10	...	...
3	0.36	0.36	1.21	0.13	2.783	1.001
4	0.36	0.36	1.45	0.15	3.059	1.280
5 <sup>a</sup>	0.48	0.52	0.91	0.10	1.708	1.059
6 <sup>a</sup>	0.48	0.52	1.64	0.23	5.196	2.725

<sup>a</sup>Refers to the cases with  $h_1 = 0.48$  m.

where  $(x, y)$  is a Cartesian coordinate system with  $x$  being the horizontal coordinate and  $y$  the upward vertical one.  $\phi(x, y, t)$  denotes the velocity potential of the fluid flow and is governed by the Laplace equation shown in Eq. (1). Equations (2) and (3) represent the kinematic and dynamic boundary conditions at the free surface  $y = \eta(x, t)$ . The

kinematic boundary condition at the bottom is given by Eq. (4) where  $b(x)$  is the bottom profile.  $g$  is the acceleration due to the gravity and subscripts denote differentiation. It should be noted that while the conditions imposed by  $\eta$  and  $\nabla\phi$  must be periodic, the periodicity of  $\phi$  is not a necessity.

The conformal mapping method realizes a transformation from the physical domain bounded by the free surface and the bathymetry into a strip (Fig. 3). With the solution of the Dirichlet boundary-value problem, a complex analytic function  $Z = X(\xi, \zeta, t) + iY(\xi, \zeta, t)$  is introduced to map the physical plane  $(x, y)$  into the mathematical one  $(\xi, \zeta)$ . The surface elevation in the mathematical plane  $Y(\xi, 0, t)$  is assumed to be periodic with  $l = 2\pi/k$ , where  $l$  is the spatial period of solution in the mathematical plane. Thus, the boundary conditions of the free surface and bathymetry profile for the function  $Y$  can be expanded in Fourier series as

$$Y(\xi, 0, t) = y(\xi, t) = \sum_{n=-\infty}^{\infty} \tilde{Y}_n e^{ink\xi} \quad \zeta = 0, \quad (5)$$

$$Y(\xi, -h, t) = b(\xi, t) = \sum_{n=-\infty}^{\infty} \tilde{B}_n e^{ink\xi} \quad \zeta = -h, \quad (6)$$

where  $\tilde{Y}_n$  and  $\tilde{B}_n$  denote the Fourier coefficients of the surface elevation and bottom bathymetry, respectively. The subscripts  $n$  represents the total number of Fourier terms. In Sec. II C, the proper number of the Fourier discrete points per wavelength has been discussed. By using the Cauchy-Riemann relations  $X_\xi = Y_\zeta$  and  $X_\zeta = -Y_\xi$ , the new general forms of  $(X, Y)$  can be easily obtained to satisfy Eqs. (5) and (6), which can be written



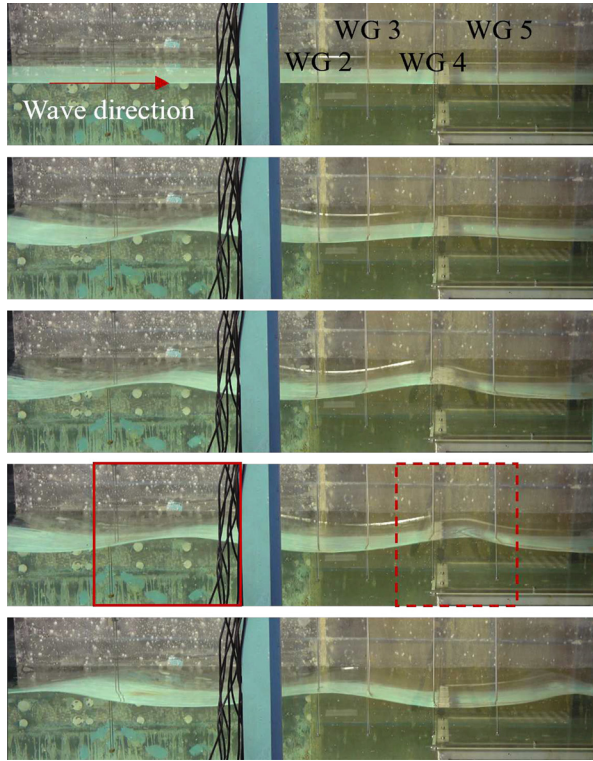


FIG. 2. Surface profiles of the monochromatic wave along with the tank at the first ADT.

$$Y(\xi, \zeta, t) = \tilde{Y}_0 + \frac{\zeta}{h}(\tilde{Y}_0 - \tilde{B}_0) + \sum_{n=-\infty, n \neq 0}^{\infty} \tilde{Y}_n \frac{\sinh nk(\zeta + h)}{\sinh nkh} e^{ink\xi} + \sum_{n=-\infty, n \neq 0}^{\infty} \tilde{B}_n \frac{\sinh nk\zeta}{\sinh nkh} e^{ink\xi}, \quad (7)$$

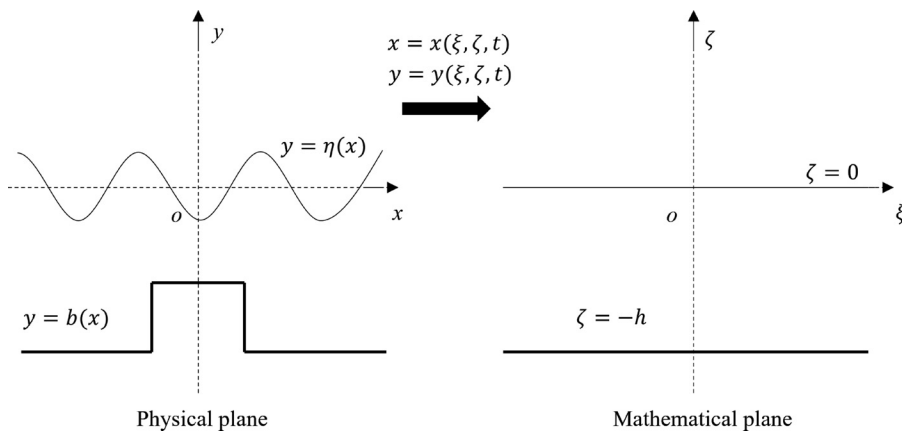


FIG. 3. The mapping transformation between the physical and the mathematical planes.

$$X(\xi, \zeta, t) = x_0(t) + \frac{\zeta}{h}(\tilde{Y}_0 - \tilde{B}_0) - \sum_{n=-\infty, n \neq 0}^{\infty} \tilde{Y}_n \frac{i \cosh nk(\zeta + h)}{\sinh nkh} e^{ink\xi} + \sum_{n=-\infty, n \neq 0}^{\infty} \tilde{B}_n \frac{i \cosh nk\zeta}{\sinh nkh} e^{ink\xi}, \quad (8)$$

where  $x_0(t)$  is the origin of the coordinate in the physical plane. Let  $h = \tilde{Y}_0 - \tilde{B}_0$  in the above equations. The first Fourier coefficient will be equal to 1, and therefore, the boundary conditions in the physical plane become periodic with the same period as in the mathematical plane. Note that the mathematical depth  $h$  is varying with time but  $b(x)$  is fixed in the computation. To further simplify the transformation between the two planes, a Hilbert-like operator is used on the harmonic conjugate variables. When  $\zeta$  tends to 0, Eqs. (7) and (8) are written as

$$x_\xi - 1 = -\tilde{h}_m[y_\xi, b_\xi], \quad (9a)$$

$$y_\xi = \tilde{h}_n[x_\xi - 1, b_\xi], \quad (9b)$$

by using the principal-value integral  $\oint$  over the real axis. The two operators  $\tilde{h}_m$  and  $\tilde{h}_n$  are

$$\tilde{h}_m[z, s] = \frac{1}{h} \oint_{-\infty}^{\infty} z(\theta) \coth[\pi(\theta - \zeta)/(2h)] d\theta + \frac{1}{h} \oint_{-\infty}^{\infty} (s(\theta) - h) \times \tanh[\pi(\theta - \zeta)/(2h)] d\theta, \quad (10)$$

$$\tilde{h}_n[z, s] = \frac{1}{h} \oint_{-\infty}^{\infty} z(\theta) \operatorname{csch}[\pi(\theta - \zeta)/(2h)] d\theta + \frac{1}{h} \oint_{-\infty}^{\infty} (s(\theta) - h) \times \operatorname{sech}[\pi(\theta - \zeta)/(2h)] d\theta, \quad (11)$$

where  $z(\theta)$  and  $s(\theta)$  denote the input functions of  $\theta$ . The two integral operators  $\tilde{h}_m[\cdot, \cdot]$  and  $\tilde{h}_n[\cdot, \cdot]$  are an inverse pair where  $\tilde{h}_m[\cdot, s] = \tilde{h}_n^{-1}[\cdot, s]$ . The same procedures are employed in terms of the velocity potential  $\phi$  and the stream function  $\psi$ , and the mapping is achieved by the operator  $\wp_s[\cdot]$ . They are obtained as

$$\phi_\xi - p = -\wp_s[\psi_\xi], \quad (12a)$$

$$\psi_\xi = -\wp_s[\phi_\xi - p], \quad (12b)$$

$$\varphi_s[z] = -\frac{1}{h} \oint_{-\infty}^{\infty} z(\theta) \operatorname{csch}[\pi(\theta - \xi)/(2h)] d\theta, \quad (13)$$

where  $p$  is the mean value of the stream function at the free-surface in the mathematical plane given by  $m[\psi]/h$ ,  $m[\cdot]$  computes the mean value over one period. Thus, the original Euler equations (1)–(4) for the surface domain  $x(\xi, 0, t)$ ,  $y(\xi, 0, t)$  and  $\phi(\xi, 0, t)$  are mapped into

$$x_t - x_\xi \left\{ \bar{h}_m \left[ \frac{\psi_\xi}{J}, 0 \right] + q(t) \right\} - y_\xi \left( \frac{\psi_\xi}{J} \right) = 0, \quad (14)$$

$$y_t + x_\xi \left( \frac{\psi_\xi}{J} \right) - y_\xi \left\{ \bar{h}_m \left[ \frac{\psi_\xi}{J}, 0 \right] + q(t) \right\} = 0, \quad (15)$$

$$\phi_t + \frac{1}{J} \left\{ \frac{1}{2} (\phi_\xi^2 - \psi_\xi^2) - J \phi_\xi \bar{h}_m \left[ \frac{\psi_\xi}{J}, 0 \right] \right\} + gy = C(t), \quad (16)$$

where  $J = x_\xi^2 + y_\xi^2$  is the Jacobian on the free surface, and  $C(t)$  is an arbitrary function of time that can be absorbed in  $\phi_t$ . The part  $q(t)$  is given by  $q(t) = m \left\{ x_\xi \bar{h}_m \left[ \frac{\psi_\xi}{J}, 0 \right] + y_\xi \left( \frac{\psi_\xi}{J} \right) \right\}$ . Therefore, the initial Euler equations in the physical plane are discretized and then mapped into the mathematical plane shown in Eqs. (14) and (15).

A pseudo-spectral method is introduced with an assumption of periodic boundary conditions. Initial surface elevations are discretized using the Discrete Fourier Transform. Given the variable nature of the bathymetry  $h(\xi, t)$ , which requires updating during the mapping process, a fixed-point iteration is initially provided. Specifically, the initial estimate  $h^{(0)}$ , derived from the most recent function value obtained in the preceding time step, is employed to update the bathymetry. The iteration can be written as

$$\Omega^{(n)} = \xi - \bar{h}_m \left[ y(\xi), h^{(n)}(\xi) \right], \quad (17)$$

$$h^{(n+1)} = b(\Omega^{(n)}), \quad (18)$$

where  $\Omega^{(n)}$  denotes the boundary condition  $X_{(\xi, h, 0)}$ . If the residue of  $|h(\Omega^{(n)}) - h(x)|$  decreases below a tolerance  $1e-10$ , the time  $n$  can proceed to the next step. Time integration is accomplished using an adaptive algorithm based on the Adams–Bashforth–Moulton method in MATLAB. The multi-step algorithm features with a strict error tolerance and a formula of order 13 is used to form the error estimate, making it suitable for problems of dynamic wave evolution.

### C. Model convergence and validation

The main tested cases are shown in Table II. It consists of two steps with the ratio  $h_2/h_1 = 0.36$  and  $0.52$ . The incident wave frequency ranges from  $0.94$  to  $1.64$  Hz. The incident wave steepness  $k_1 a$  was carefully selected and tested to make sure the effects on the higher harmonics can be captured. For all the tested cases with the step in the wave flume, we have also generated pure waves without the step. This is to ensure we can obtain accurate information on the incident wave. The physical amplitude  $a$  has been modified with the experiments on the constant depth seen in Appendix A).

This section presents the numerical setup and the validation with experimental measurements. In the pre-processing, the equations are nondimensionalized by using  $g$  as unit acceleration and  $h_1$  as unit length. Thus, the two dimensionless input parameters, amplitude and wavelength, are  $a/h_1$  and  $L/h_1$ . In this case, the dimensions in the numerical simulation have been reduced. This pre-processing is

required before analyzing the numerical results. In the fully nonlinear numerical model, an absorbing condition is added to minimize the influence of periodic boundary conditions. A linear damping is implemented by a shape function which reduces the velocity potential at the right boundary; hence, rare influence will be on the surface waves propagating from the left side.<sup>46</sup>

To verify our numerical model, wave profiles propagating over a shoal arising from the experimental measurements, numerical simulations using a high-order spectral method (HOSM) and numerical simulations using the conformal mapping method are compared in Figs. 4(a) and 4(b) at four different positions. Overall, the simulated data show good agreement with the numerical and experimental results. There are small discrepancies in the trough as can be seen in Figs. 4(c) and 4(d). This can likely be attributed to the effects of bottom friction and dissipation from the sidewalls.

To capture strong nonlinearities during wave evolution, a sufficient number of Fourier terms or points per wavelength should be used in numerical simulations. The variation of surface elevations  $\eta$  is shown in Fig. 5 with six different numbers (10–70) of Fourier discrete points per wavelength. The wave profiles over two wave periods indicate that the results with 31 to 69 discrete numbers show good agreement. These wave profiles are highly nonlinear because they are located on the shallower region ( $x = 12.05$  and  $13.82$ ), which shows the capability of the numerical model for fully nonlinear simulations. In this study, 52 Fourier terms are chosen for the investigation of the wave evolution over the varying bathymetry. Further study of numerical convergence for higher harmonics is demonstrated in Appendix A.

To validate the model, the nonlinear wave evolution for case 1 with a step of  $h_2/h_1 = 0.36$  is compared between the experimental measurements and numerical simulations in Fig. 6. The surface elevations at the 8 wave gauges are all shown in a time window covering 16 s. The agreement between the simulated and measured profiles is excellent. The characteristics of the surface elevations compare well with that of the experiments, especially for the sharp crests and flat troughs. We see that the wave is nearly linear at WG 1 and the nonlinearity increases in front of the step at WG 2–4. Near the center of the step, the nonlinearity becomes much stronger with distorted surface shapes. Note that there are discrepancies in the initial stage at each wave gauge position. The transient part at the beginning of the measurements is due to the build-up of the physical wavemaker motion, which is not modeled in the numerical simulations. Moreover, the comparison of wave profiles achieved by the experiments and numerical simulation is presented in Fig. 7. The measured data on the constant depth also well validate the numerical model. The possible unphysical flat crests in several measurements might be due to the unstable wave gauge performance. In all our tests, we repeated three times to reduce errors as possible. In terms of computing reflection coefficients and spectral analysis of higher harmonics, comparisons in Secs. III A–III C show that these might have minor effects on the linear reflection coefficient, and higher harmonics are not much influenced.

## III. RESULTS AND DISCUSSION

### A. Higher harmonic wave elevations

This section presents the harmonic wave amplitudes of the experimental measurements and numerical simulations in the frequency and time domains. To access the wave nonlinearity induced by the

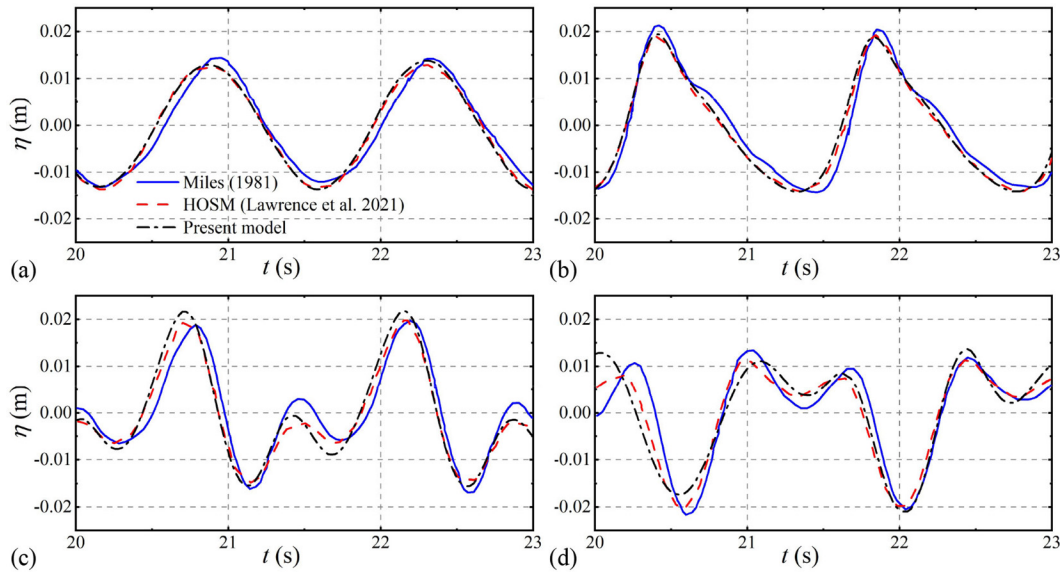


FIG. 4. Surface elevations over a shoal<sup>45</sup> with  $f_0 = 0.70$  Hz,  $a = 0.0135$  (a)  $x = -1.57$ , (b)  $x = -0.35$ , (c)  $x = 1.42$ , and (d)  $x = 2.45$  m.

abrupt depth transitions, the harmonic amplitudes are nondimensionalized by the incident wave amplitude measured at WG 1. In addition, all the tested cases refer to waves propagating over finite water depths with a time window of 10–30 s. This time window ensures sufficient wave records for a stationary state over the submerged step and no disturbance from the reflected waves from the end of the wave tank. The selection of the time window is detailed in Appendix A.

Figures 8 and 9 present the variation of reflection coefficients with increasing  $k_1 h_2$  and steepness  $k_1 a$ . The wave reflection considers the linear and the second harmonics, respectively. The computation of the reflection coefficients with measured and numerical data is different. The experimental coefficients are obtained using an improved Goda's method (two wave gauges), while the numerical simulations employ four wave gauges.<sup>47,48</sup> The relative water depth  $k_1 h_2$  ranges from 0.35–0.70 for  $h_2/h_1 = 0.36$  and from 0.5–2.0 for  $h_2/h_1 = 0.52$ . When compared with the theory of Loukili *et al.*,<sup>49</sup> a good comparison can be found with the reflection coefficients obtained with numerical simulations and experiments. Meanwhile, the theoretical results from Mei *et al.*<sup>28</sup> have also validate the numerical results and Loukili's theory with long waves. The observed shift between the

numerical and theoretical models is attributed to the distinct impacts of bottom and free-surface nonlinearities on frequency.<sup>50</sup> These discrepancies arise from the assumption of a small wave amplitude in Loukili *et al.*'s<sup>49</sup> study. In contrast, this study employs a higher wave steepness. Specifically, bottom nonlinearity instigates a downshift, while free-surface nonlinearity provokes an upshift. The frequency shifts exhibit a quadratic dependence on steepness, inducing more pronounced upshifts. Thus, an increase in wave steepness augments nonlinearity. The increased incident steepness,  $k_1 a$ , has a minor effect on the values of reflection coefficients. This could explain the slight discrepancy in coefficient values, rather than the trend of variation with increasing  $k_1 h_2$ .

The second components can be further categorized into bound (locked mode) and free waves.<sup>51</sup> The free waves propagate at their individual phase velocities as dictated by the dispersion relation. Due to the minor frequency difference between free and bound waves, separation from the spectrum using fast Fourier transform (FFT) is insufficient. The amplitudes of the second bound and free waves are separated using the four wave gauges method to study the reflection and transmission of superharmonics.<sup>48</sup> Tables III and IV present the

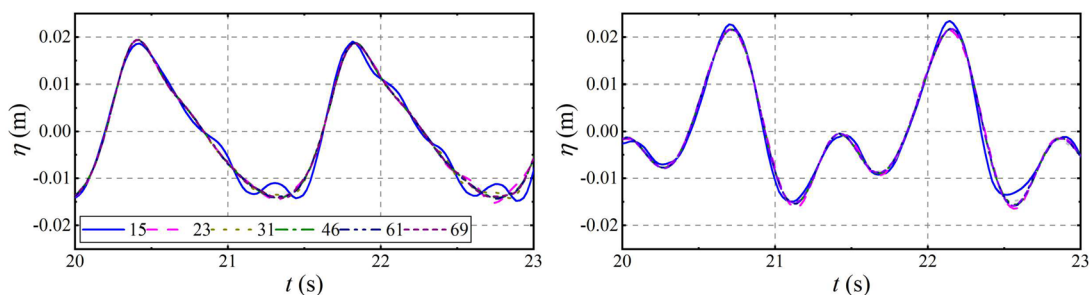
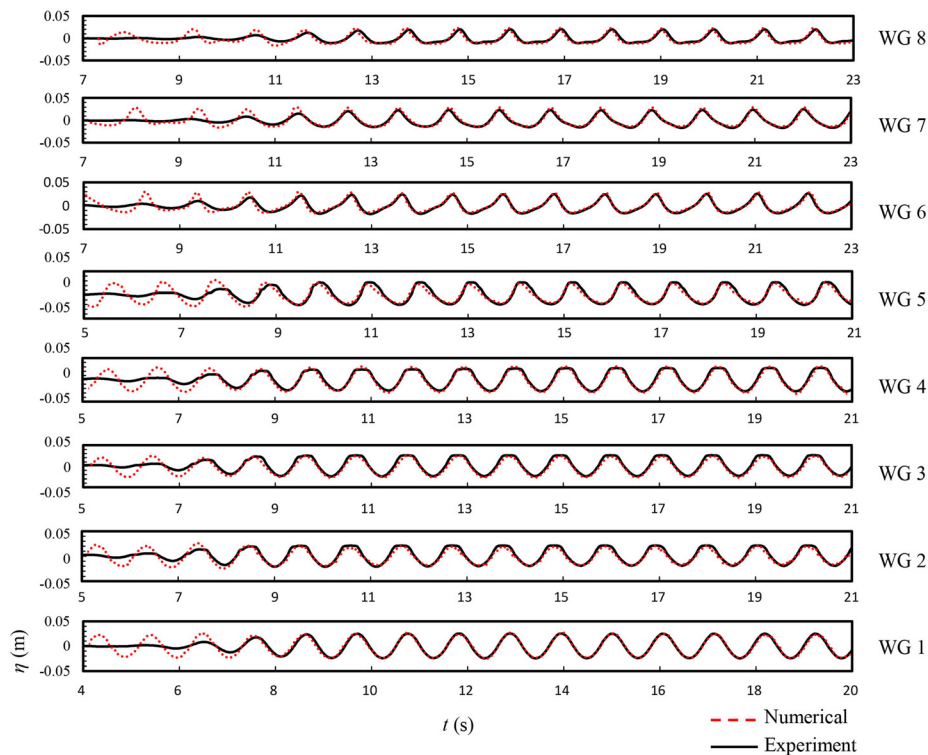


FIG. 5. Model convergence with different numbers of Fourier terms per wavelength: (a)  $x = -0.35$  and (b)  $x = 1.42$  m.



**FIG. 6.** Comparison of experimental measurements and numerical results for the surface elevation at the 8 wave positions along the tank for case 1  $f_0 = 0.94$  Hz,  $k_1 a = 0.06$ .

results of transmission coefficients considering only the first and the sum of the first two harmonics. The transmission coefficients are defined as the ratio of the amplitude of transmitted waves to that of incident waves. The parameter  $E_1$  is calculated as  $E_1 = K_{r1}^2 + K_{t1}^2$ , considering only the linear components. The position of the surface elevation of transmitted waves is chosen to be approximately two wavelengths after the second abrupt depth transition. A detailed

description of the separation method is presented in [Appendixes B and C](#).

Concerning the nonlinear effect, another parameter  $E_{1,2}$  is defined as the sum of the first and second harmonic coefficients,  $E_{1,2} = K_{r1,2}^2 + K_{t1,2}^2$ . We see that  $E_1$  is close to 1 for most cases, and  $E_{1,2}$  is significantly less than 1, nearly half of  $E_1$ . Regarding the second harmonic waves, there are seldom any second components in the incident waves. However, the existence of abrupt depth triggers superharmonics. As mentioned before, bound waves dissipate after propagating over the second depth transition, but free waves continue to evolve forward. The reflection coefficients are nearly identical whether considering only the first harmonic wave or both the first and second harmonic waves. However, considering second harmonics might lower the value of coefficients  $K_{t1,2}$  and  $E_{1,2}$ .

[Table V](#) shows the components of the second order, including the second superharmonics (two points method) and the second free and bound waves (four points method). It is observed that the amplitudes of the isolated second bound  $A_{I,B}^2$  and free waves  $A_{I,F}^2$  surpass those of the general second harmonic components  $A_I^2$ . A disparity is also noticeable when comparing the ratio of reflected to incident waves, but it is found that the value of second components  $A_R^2/A_I^2$  is closer to the free waves  $A_{R,F}^2/A_{I,F}^2$ . This may be attributed to that the generation of superharmonics is predominantly concentrated in regions characterized by abrupt depth transitions and shallower areas, leading to less reflection before the step.

The energy spectra (in log scale) of the surface elevations for four cases are shown in [Fig. 10](#), where the latter two cases refer to the case with  $h_2/h_1 = 0.52$ . [Figure 10\(a\)](#) describes the energy spectra of the numerical results at four different wave gauge positions with two

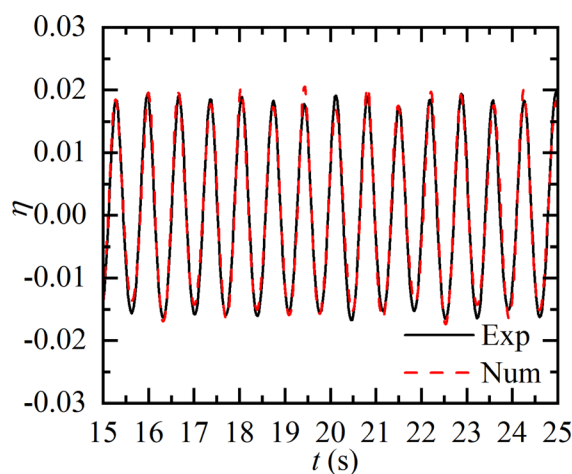


**FIG. 7.** Comparison of wave profiles on the condition with the constant depth for case 4  $f_0 = 1.45$  Hz,  $k_1 a = 0.15$ .



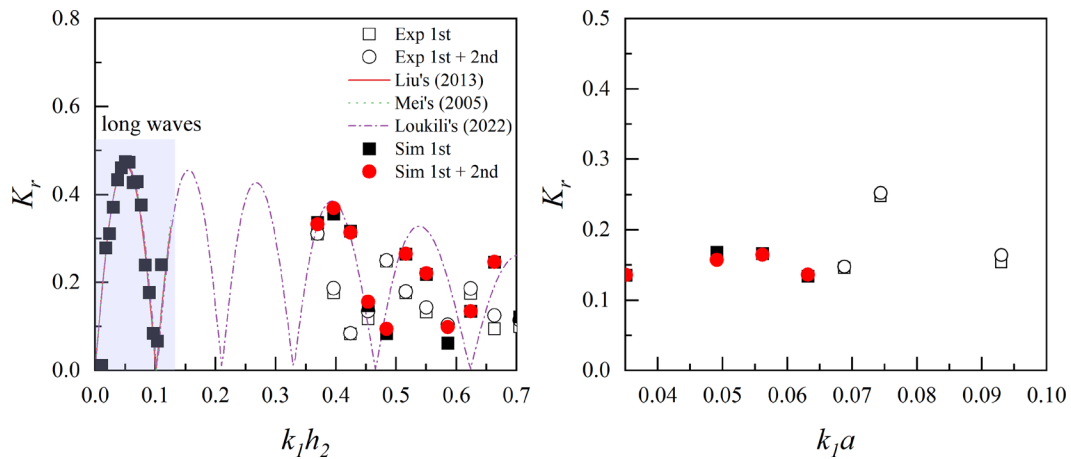


FIG. 8. Reflection coefficients as a function of  $k_1 h_2$  and amplitude  $k_1 a$  with  $h_2/h_1 = 0.36$ .

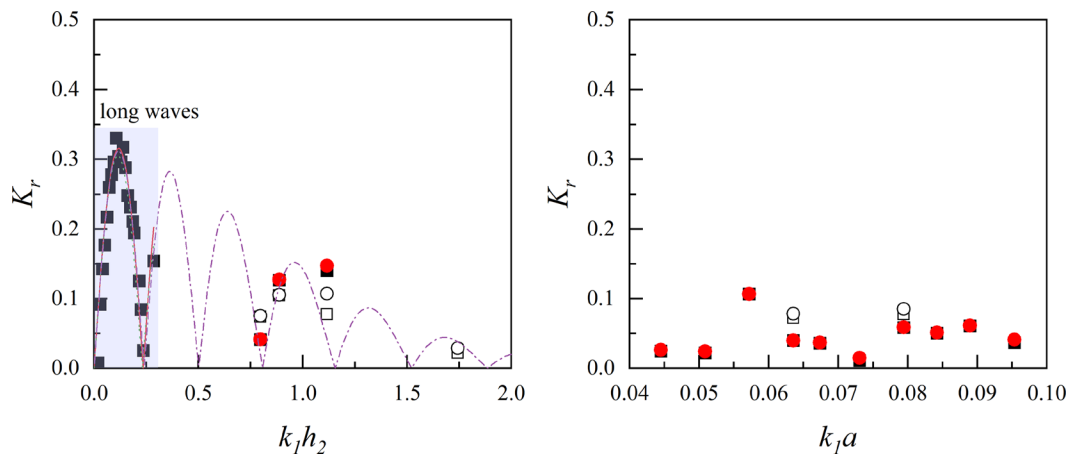


FIG. 9. Reflection coefficients as a function of  $k_1 h_2$  and amplitude  $k_1 a$  with  $h_2/h_1 = 0.52$ .

TABLE III. Reflection and transmission coefficients for the linear and the first two harmonic components with varying  $k_1 h_2$ .

$f_0$ (Hz)	$k_1 h_2$	$a$	$k_1 a$	$K_{r1}$	$K_{r1,2}$	$K_{t1}$	$K_{t1,2}$	$E_1$	$E_{1,2}$
0.74	0.370	0.018	0.05	0.337	0.332	1.026	0.678	1.165	0.570
0.78	0.396	0.011	...	0.356	0.369	1.035	0.816	1.200	0.802
0.82	0.424	0.015	...	0.317	0.314	1.032	0.742	1.166	0.649
0.86	0.453	0.014	...	0.147	0.156	1.093	0.771	1.217	0.619
0.90	0.484	0.013	...	0.084	0.095	1.075	0.761	1.162	0.588
0.94	0.516	0.015	0.06	0.265	0.265	1.043	0.758	1.158	0.645
0.98	0.550	0.014	...	0.218	0.221	1.036	0.750	1.121	0.611
1.06	0.624	0.015	0.07	0.135	0.135	1.047	0.742	1.114	0.569
1.10	0.664	0.014	...	0.246	0.247	0.981	0.695	1.023	0.543
0.85*	0.797	...	0.060	0.041	0.041	1.000	0.705	1.000	0.705
0.91*	0.888	...	0.068	0.127	0.128	0.997	0.706	1.009	0.515
1.04*	1.116	...	0.085	0.140	0.148	0.978	0.691	0.976	0.499

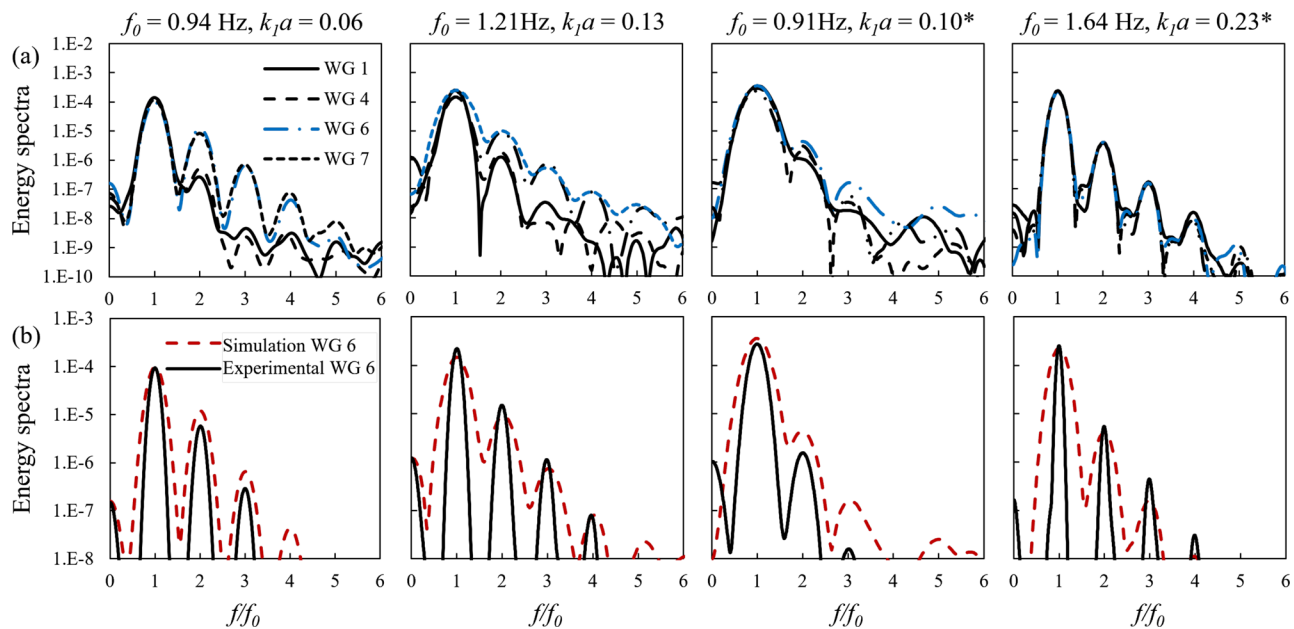
before the step (WG 1 and 4) and two above the step (WG 6 and 7). In terms of the wave energy in front of the step (WG 1 and 4), it is found that the values at the first harmonic  $1 \cdot f_0$  are similar and just over  $1 \times 10^{-4}$ . Then, the energy at  $2 \cdot f_0$  is about two orders of magnitudes smaller than that at  $1 \cdot f_0$ . The energy at  $3 \cdot f_0$  is less than  $1 \times 10^{-7}$  and that of the  $4 \cdot f_0$  component is even two orders of magnitude smaller, which can be ignored. A great difference is found between the wave energy before and above the step in the case  $h_2/h_1 = 0.36$ . Specifically, the wave energy at  $2 \cdot f_0$  is one to two orders higher than that before the step. The maximum increase of  $3 \cdot f_0$  is 3 orders of magnitude in the case  $f_0 = 0.36$  Hz,  $k_1 a = 0.06$ . Figure 10(b) compares the wave energy of measurements and numerical simulations at WG 6. They show good agreement for the values at the harmonic frequencies. Here, the harmonic analysis shows that the ADT effectively enhances the wave energy of superharmonics on the shallower regions (WG 6 and 7) on the step, especially for the second and third harmonics. Second, since there is no obvious change in the superharmonic amplitudes at the ADT (WG 4), a possible explanation

**TABLE IV.** Reflection and transmission coefficients for the linear and the first two harmonic components with varying  $k_1 a$ .

$f_0$ (Hz)	$k_1 h_2$	$a$	$k_1 a$	$K_{r1}$	$K_{r1,2}$	$K_{t1}$	$K_{t1,2}$	$E_1$	$E_{1,2}$
0.86	0.455	0.010	0.035	0.135	0.136	1.085	0.765	1.194	0.604
...	...	0.014	0.049	0.147	0.156	1.093	0.771	1.217	0.619
...	...	0.016	0.056	0.166	0.164	1.082	0.759	1.198	0.602
...	...	0.018	0.063	0.134	0.136	1.035	0.7221	1.089	0.540
0.85*	0.595	0.010	0.032	0.088	0.088	1.013	0.716	1.034	0.521
...	...	0.014	0.045	0.025	0.026	1.005	0.710	1.011	0.505
...	...	0.016	0.051	0.022	0.024	1.007	0.711	1.015	0.506
...	...	0.018	0.057	0.107	0.107	1.010	0.714	1.031	0.520
...	...	0.020	0.064	0.040	0.040	1.003	0.708	1.007	0.503
...	...	0.0212	0.067	0.036	0.037	1.006	0.710	1.013	0.505
...	...	0.023	0.073	0.011	0.015	1.003	0.707	1.005	0.500
...	...	0.025	0.079	0.058	0.059	1.003	0.708	1.010	0.505
...	...	0.0265	0.084	0.050	0.051	1.001	0.706	1.004	0.501
...	...	0.028	0.089	0.061	0.061	0.996	0.703	0.995	0.498
...	...	0.030	0.095	0.038	0.041	1.001	0.707	1.004	0.502
...	...	0.035	0.111	0.079	0.079	0.962	0.682	0.932	0.472

**TABLE V.** The separated free and bound components in three different cases.

$f_0$ (Hz)	$k_1 a$	$A_I^2$ (mm)	$A_R^2$ (mm)	$A_{I,B}^2$ (mm)	$A_{R,B}^2$ (mm)	$A_{I,F}^2$ (mm)	$A_{R,F}^2$ (mm)	$A_R^2/A_I^2$	$A_{R,B}^2/A_{I,B}^2$	$A_{R,F}^2/A_{I,F}^2$
0.94	0.06	0.824	0.192	3.836	1.059	2.664	0.707	0.233	0.276	0.265
1.06	0.07	0.851	0.376	2.352	0.216	1.303	0.514	0.442	0.092	0.395
0.91*	0.10	1.407	0.324	3.277	0.613	1.608	0.710	0.230	0.187	0.442

**FIG. 10.** (a) Results of energy spectrum along the step and (b) comparison of experimental measurements and numerical simulation on WG 6.

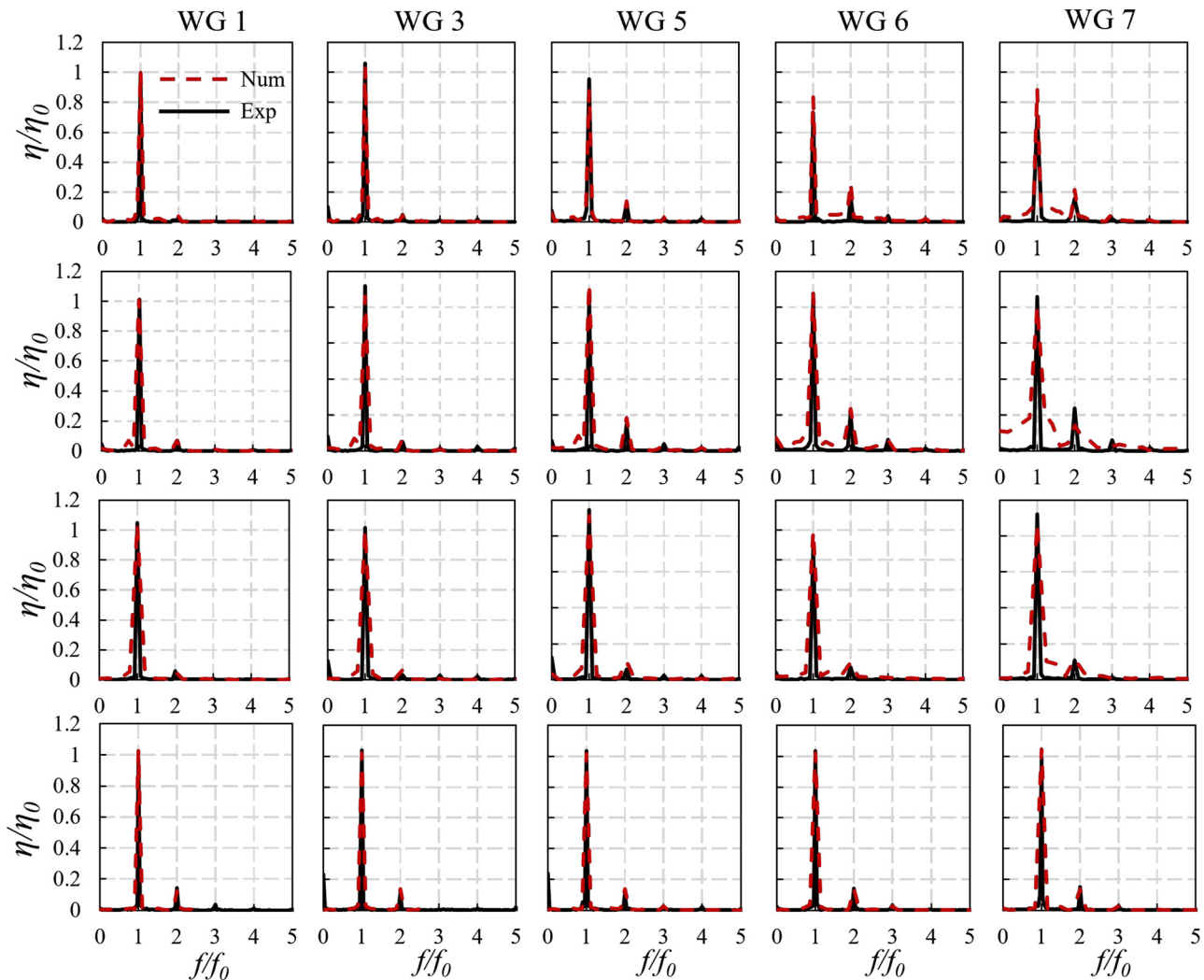


FIG. 11. Discrete amplitude spectra of the surface elevations measured at the different gauge positions in the experiments compared to the numerical results in cases 1, 2, 5\*, and 6\* (\* refers to  $h_2/h_1 = 0.52$ ).

transition. Consequently, a possible explanation for the enhancement of the superharmonic amplitudes is an energy transfer from the first harmonic to the superharmonics induced by the abrupt depth transitions. Indeed, Mei and Unluata<sup>52</sup> suggested that the energy could be transferred from the first harmonic to the higher harmonics.

To illustrate the harmonics propagating over the submerged step, Fig. 12 describes the normalized total surface elevation  $\eta/\eta_0$  and the first to third harmonic evolution  $\eta_m/\eta_0$  ( $m = 1, 2, 3$ ) at four wave gauge positions (case 1). The time windows (14–18 s) are properly chosen where the waves have passed over the submerged step but with no disturbance from the reflected waves. The separated harmonics are obtained by the FFT and inverse FFT (IFFT) of the surface elevations at each wave gauge position. For the first harmonic amplitude, no clear difference is observed on WG 1 and 5. However, the amplitudes are reduced by about 33% on WG 6 and 7. By contrast, there is a clear increase in the second and third harmonic amplitudes on top of the

submerged step (WG 5, 6 and 7) where the amount increases up to 2–3 times that on WG 1. The superharmonic amplitudes on WG 7 are slightly smaller than those on WG 6. This will be further discussed in Sec. III B. To sum up, except for the decrease in the first harmonic, the ADT effectively increases the superharmonic amplitudes on the shallower regions on the step, which is consistent with the recent study of Draycott *et al.*<sup>38</sup> Moreover, the free-surface elevations on WG 6 and 7 with sharper crests and flatter troughs further demonstrate the strong effects of the sudden water depth transitions on wave nonlinearity.

## B. Higher harmonic wave profiles

The spatial characteristics of the measured and simulated waves over the abrupt depth transitions are discussed in this section. Figure 13 displays the spatial evolution of wave profiles over a distance of 15 m with numerical simulations for four selected cases. ( $x, \eta/\eta_0$ ) is

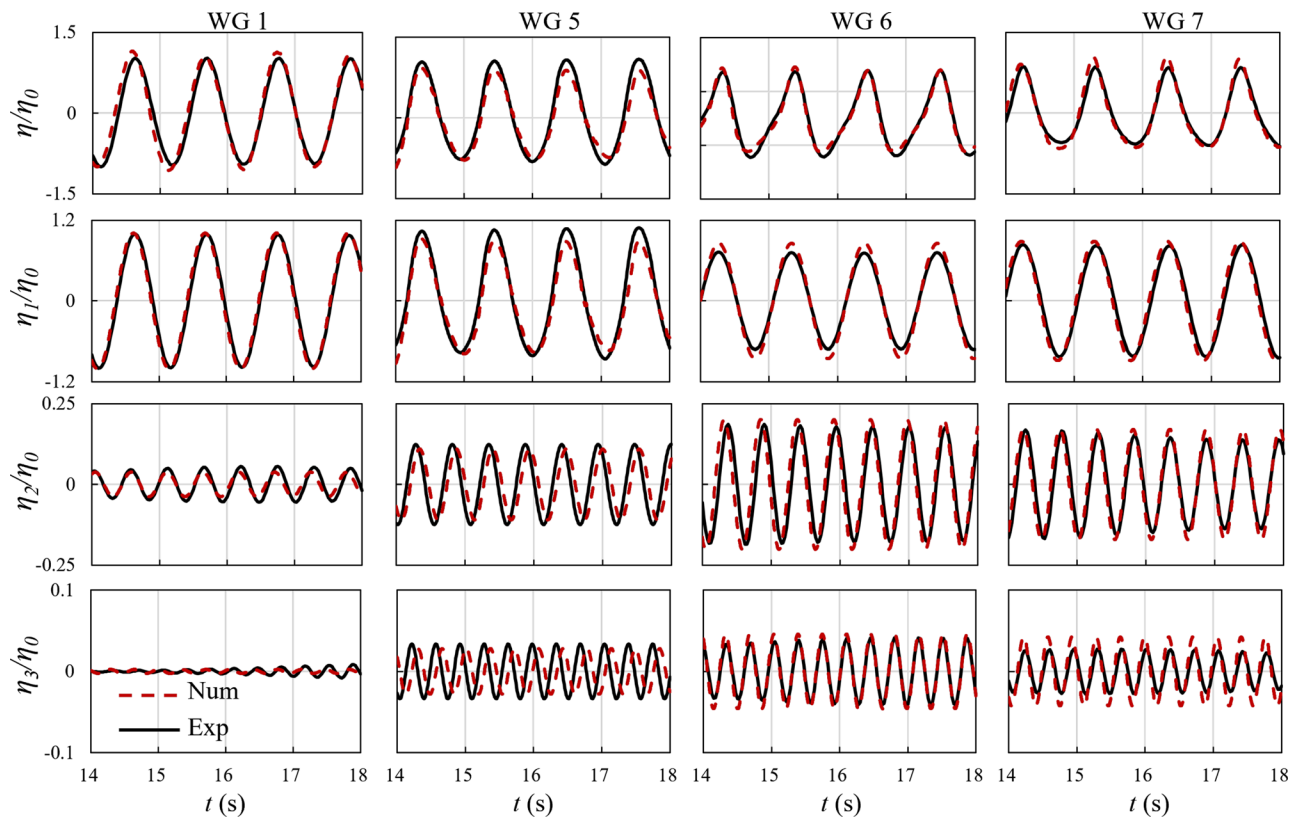


FIG. 12. Comparison of separated harmonic time series for case 1 showing experimental and numerical results at several gauge positions.

a Cartesian coordinate system where the left vertical axis  $\eta/\eta_0$  shows the normalized surface elevation and the right axis indicates the time in seconds. In the simulations, the steady state is achieved after about 5 s. For the case  $f_0 = 0.94$  Hz with the water depth ratio  $h_2/h_1 = 0.36$ , the depth change is relatively large at the first ADT such that linear dispersion relation might dominate the wave profile change for a nondeep water wave. We can see the profile distortion on the step and behind the step at 5 s, which is consistent with the study of Massel.<sup>27</sup> A similar trend is observed for  $f_0 = 1.21$  Hz though it is a shorter wave. The distortion and large profile transformation of waves over an ADT has been reported by several authors.<sup>53,54</sup> For the larger water depth ratio  $h_2/h_1 = 0.52$ , the profile transformation over the ADT seems not that significant, due to the smaller change of wavelength over the ADT. Again, the wave profiles show a reduction of amplitudes behind the step, which is consistent with the observations in Fig. 11. We see that the complex wave evolution exhibits the strong effect of the small ratio of the water depths on the wavelengths, especially for the cases with long wavelengths. It results in clear nonlinear wave profiles on the shallower region and longer wavelengths at the back side of the step.

Figure 14 displays the normalized surface elevations and the first three superharmonic amplitudes in space for cases  $f_0 = 0.94$  Hz with wave steepness  $k_1 a = 0.06$  and  $0.1$  on water depth  $h_2/h_1 = 0.36$ . The experimental and computed results show a good agreement for the higher harmonics in both cases. To extract the superharmonics in

space, the surface elevations at each position are calculated with the FFT. The same time windows are used for the elevation signals. The start points of the time windows 16.2 and 16.6 s are chosen when three to four wavelengths have passed over the first ADT. It can be found that the crest with the higher wave steepness ( $k_1 a = 0.1$ ) is sharper in the middle of the step. In terms of the first harmonic amplitude, it is observed that the normalized surface elevations  $\eta_1/\eta_0$  decrease along the submerged step in both cases. The normalized amount of the crest of the first harmonic is about 1.1 times the linear components. However, it has decreased to 0.84 after propagating over the submerged step ( $x > 1.2$  m). The result is mainly attributed to the wave reflection at the first ADT, leading to a partial transmission of the waves over the step. The amplitudes of the second harmonic on the shallower regions are about 20% of that of the first terms but this amount is 2–3 times larger than that on the deeper side ( $x = -2.2$  m). Similarly, there are relatively larger components of the third harmonic waves focusing on the shallower regions on the step. Notably, the third harmonics in front of the step is much smaller and negligible. The profiles of the second and third harmonic waves for the second case are similar to those for the first, except that the third harmonic is twice higher than the first. There is a small discrepancy in the measured and simulated results in the second case at  $x = 0$  on the step attributed to the disagreement at the second harmonic. The overall agreement between the experiments and the numerical results is excellent.



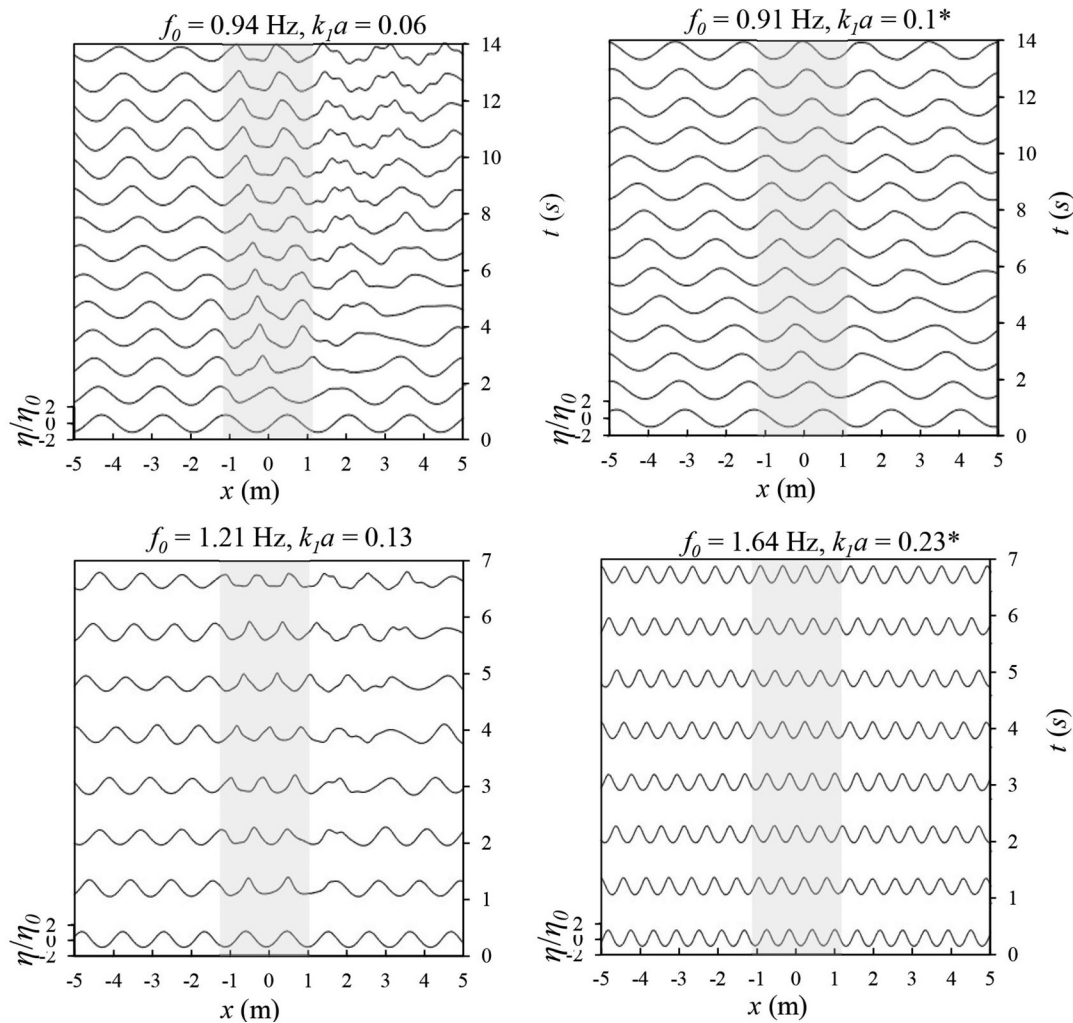


FIG. 13. Wave evolution along the submerged step of several incident wave cases with numerical simulations (\* refers to  $h_2/h_1 = 0.52$ ).

The normalized amplitudes of the first to fourth harmonics in the spatial domain are presented in Fig. 15 for six selected cases. The y axis refers to the ratio of harmonic amplitude to the incident wave amplitude; the x axis is the spatial range where the location of the step is from  $-1.2$  to  $1.2$  m (seen in the shaded area). The experimental results agree with those of the numerical simulations. For the cases of the water depth with  $h_2/h_1 = 0.36$ , a clear decrease in the first harmonic amplitude is found along the submerged step. For instance, the first harmonic amplitude at the second ADT ( $x = 1.2$  m) is  $0.4$  smaller than that at the first ADT ( $x = -1.2$  m) in case 1 with  $f_0 = 0.94$  Hz and  $k_1a = 0.06$ . Then, the amplitude keeps decreasing and becomes only half of that at  $x = 2.5$  m. With a larger steepness  $k_1a = 0.1$ , the first harmonic amplitude decreases at the first ADT but returns before the second ADT (at  $x = 1.0$  m) and reaches  $2/3$  of the incident amplitude at  $x = 2.5$  m. The features of the first harmonic are the result of reflection by the submerged step and the interaction of the incident wave with the reflected wave. A linear model is able to capture the local

variations on the step. By contrast, the second harmonic amplitudes increase on the shallower regions for all the cases with the water depth  $h_2/h_1 = 0.36$ . The fluctuations of the second harmonic are stronger than that of the first harmonic, but their amplitudes can grow up to  $2$ – $5$  times at the front side of the step. Strong effects on the second harmonics can be observed in case 2 with  $f_0 = 0.94$  Hz,  $k_1a = 0.1$ . For the cases with higher incident frequency ( $f_0 = 1.21$  and  $1.45$  Hz in Fig. 15), the amplitudes of the second harmonic are much lower on the step since the influence of the abrupt depth transitions is less significant for the waves with shorter wavelengths.

The third and fourth harmonic amplitudes have been found to have the same trend for oscillations as that of the second. For the case  $f_0 = 0.94$  Hz, the amplitudes of the third harmonic are about  $30\%$ – $40\%$  of that of the second harmonic and the fourth harmonic is nearly zero which can be ignored. The amplitudes of these two superharmonics grow at the first ADT and vary regularly on the shallower region. Both amplitudes return to the incident conditions after propagating over the

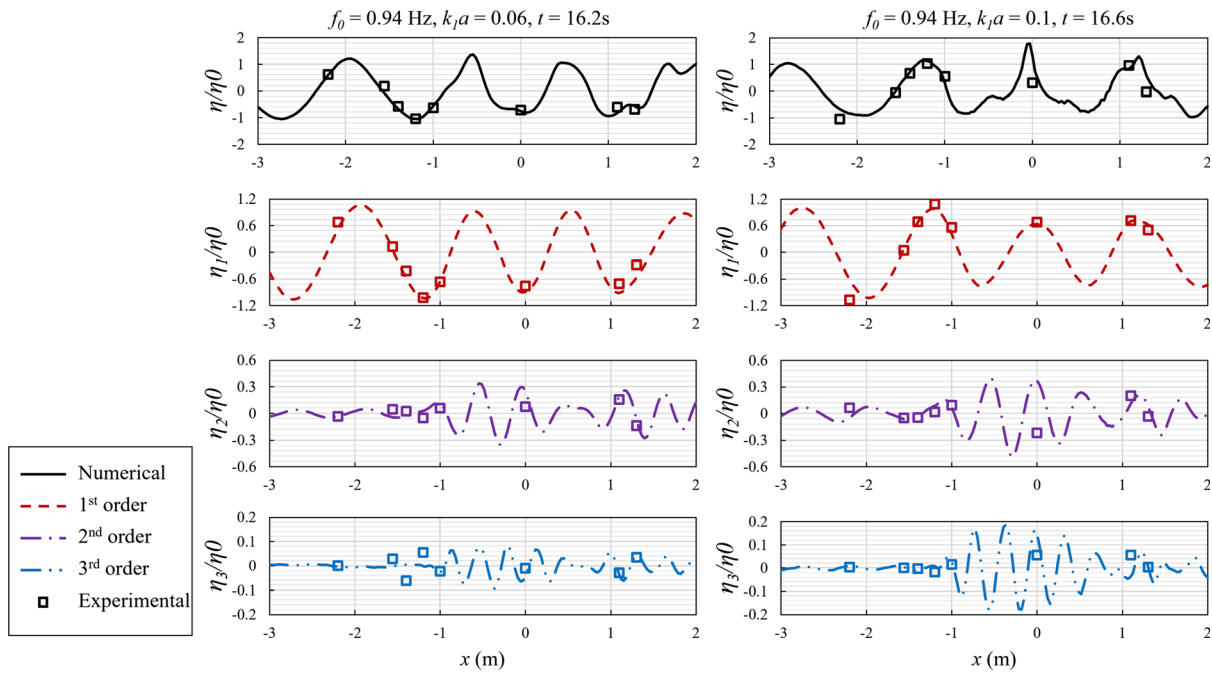


FIG. 14. Separated harmonics from numerical simulations as a function of space and compared to experiments for two selected cases at the wave gauges.

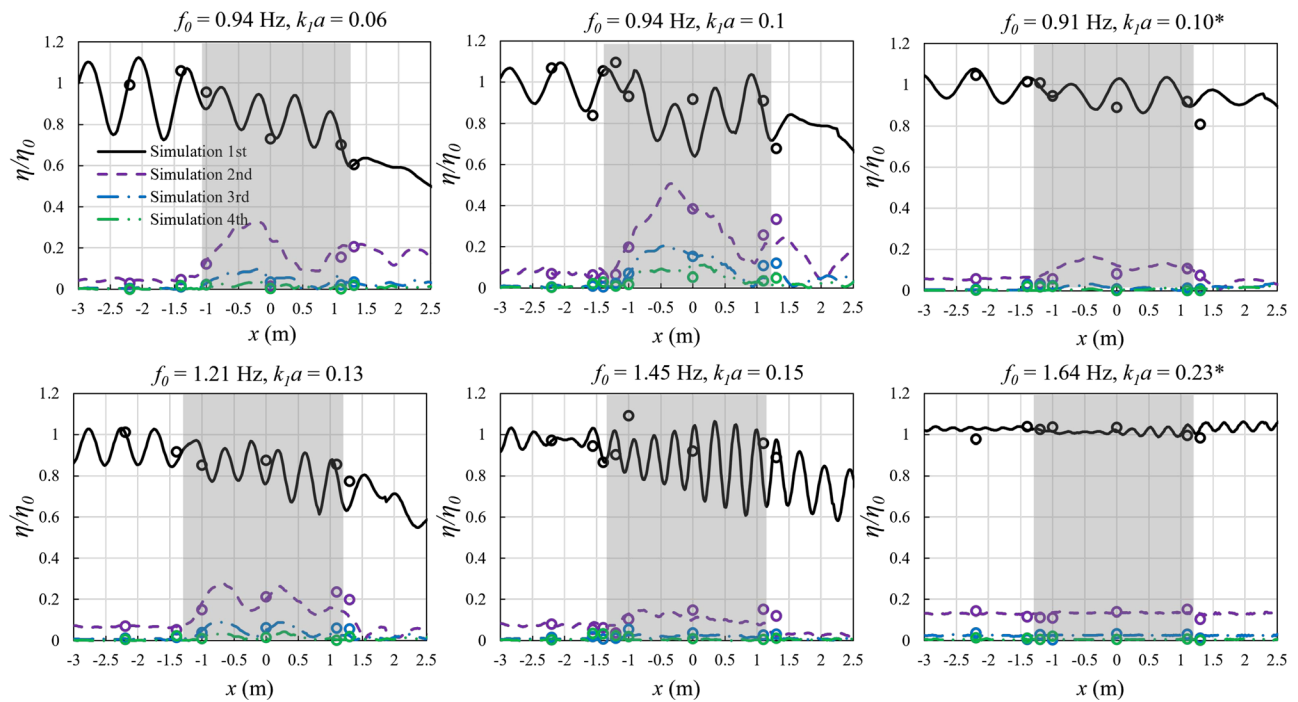


FIG. 15. Spatial distribution of the amplitude of wave harmonics for selected cases (\* refers to  $h_2/h_1 = 0.52$ ). Lines: numerical data; Circles: experimental data.

second ADT. For the water depth  $h_2/h_1 = 0.52$ , the evolution of the superharmonics is similar to that in the water depth  $h_2/h_1 = 0.36$ . Consequently, the abrupt depth transitions reduce the first harmonic amplitude resulting from the wave partial reflection. The superharmonic amplitudes increase suddenly at the first ADT and remain high on the step, and their amplitudes decrease after the second ADT, making the superharmonics localized on the step. These results are attributed to a smaller influence of the abrupt depth transitions, leading to smaller reflection coefficients of the superharmonics, which agrees well with the findings in Christou *et al.*<sup>55</sup> It can be concluded that the influence of the water depth ratio is dominant on the induced higher harmonics and the nonlinear effect due to the incident wave steepness in general plays a less important role in this case. It is noteworthy that the second harmonic amplitude can reach the same magnitude as that of the first harmonic (in case  $2f_0 = 0.94$  Hz,  $k_1 a = 0.1$ ), which was also reported in the work of Draycott *et al.*<sup>38</sup> They confirmed that the wave breaking on the top of the step was attributed to the second harmonic terms being higher than that of the first harmonic.

### C. Nonlinear effect with varying wave parameters

To further study the nonlinear effects on the waves over a submerged step, this section presents the results of experiments and numerical simulations with varying water depth, wave frequency and wave steepness.

Figure 16 displays the variation of the harmonic amplitudes for the cases with two water depth transitions  $h_2/h_1 = 0.36$  and  $h_2/h_1 = 0.52$  with a range of incident wave frequencies  $k_1 h_1$ . The experimental and numerical results show good agreements for both the first and second harmonics at the selected wave gauge positions. Figure 16(a) shows the nondimensionalized amplitudes of the first and second harmonics with  $k_1 h_1 = 1$ –2 for  $h_2/h_1 = 0.36$  and  $H = 0.03$  m. It can be found that the mean amplitudes of the first harmonic are about 1 at the locations in front of the first ADT (WG 3 and 5), though the amplitude variation at WG 5 is slightly higher presumably due to the influence of reflection at the submerged step. The second harmonic components remain low for all  $k_1 h_1$  values, which is expected since the

nonlinearity in the incident wave is not significant. On the step at WG 6 and WG 7, the amplitudes of the first harmonic are mostly less than 1, attributed to the reflection at the step. However, the second harmonic components become significantly larger especially when  $k_1 h_1 < 1.5$ . In Sec. III B, the higher harmonics induced by the step were shown to be triggered by the ADT for waves with longer wavelengths. For  $k_1 h_1 > 1.5$ , the nonlinear effect at the step becomes less important hence the second harmonics reduce to less than 0.2.

In contrast, the results for the case  $h_2/h_1 = 0.52$  in Fig. 16(b) illustrate that a weaker nonlinear effect is present in deeper water depth. Note that the incident wave heights are slightly larger with  $H = 0.04$  m. The variations of the first and second harmonics are small in the entire range of  $k_1 h_1$  ( $k_1 h_1 = 1$ –7). Except for a small variation when the wavelength is long ( $k_1 h_1 < 1.5$ ), the first harmonic amplitudes are near 1 for all four wave gauges. The second harmonics remain low, except for small values of  $k_1 h_1$ . The results with varying wave frequencies ( $k_1 h_1$ ) for the two water depths demonstrate again that wave dispersion dominates the nonlinear effects at the abrupt depth transitions for relatively long waves. In addition, our nonlinear numerical model shows robustness across the shallow and deep water regions.

We now examine the nonlinear effects associated with increased wave steepness. In Fig. 17, the superharmonic amplitudes are shown with increasing  $k_1 a$  (0.03–0.1) for  $f_0 = 0.86$  Hz on the two water depths. Both measurements and numerical results are plotted. The overall agreement between the experiments and numerical simulations is acceptable. Note that the first harmonics are not shown here which are close to 1 for all the cases. It is found that generally the nondimensional superharmonics increase with steepness at the selected wave gauge positions. The nondimensional elevations on WG 6 at the step center are mostly the highest as expected. Note that there is a slight drop in the second harmonics when the input wave steepness is larger than 0.09 in the case with  $h_2/h_1 = 0.36$ . There is a disagreement for the second harmonics between the experimental and the numerical results on WG 7. A possible reason is that there might be an influence of the second free waves when the nonlinearity increases.<sup>55</sup>

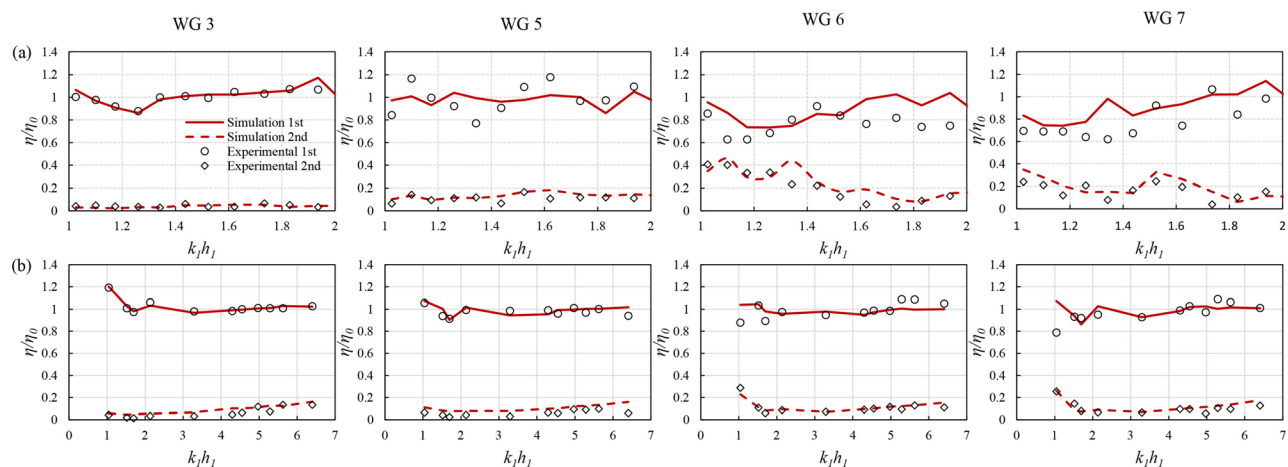
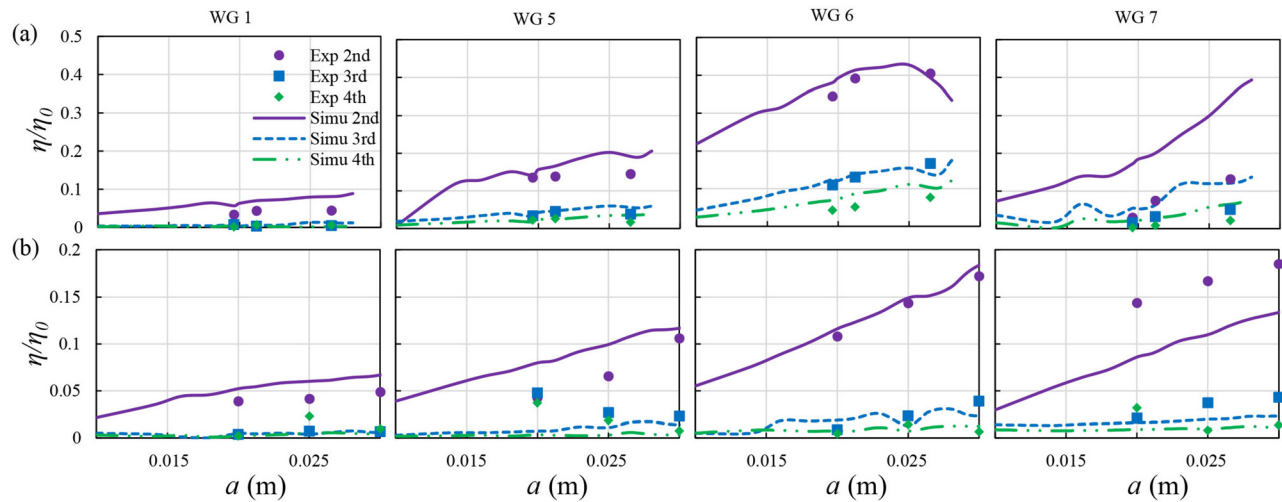


FIG. 16. Normalized amplitudes of the first and second harmonics over the different gauge positions on two water depths with (a)  $h_2/h_1 = 0.36$ ,  $H = 0.03$  m and (b)  $h_2/h_1 = 0.52$ ,  $H = 0.04$  m.



**FIG. 17.** Extracted higher harmonic amplitudes at different gauge positions as a function of input amplitude  $k_1 a$  comparing experiments and numerical simulations for the case  $f_0 = 0.86$  Hz: (a)  $h_2/h_1 = 0.36$  and (b)  $h_2/h_1 = 0.52$ .

For the case  $h_2/h_1 = 0.52$ , steeper waves also induce larger higher harmonics but with smaller amplitudes of these harmonics than that for  $h_2/h_1 = 0.36$ . The increasing incident wave steepness effectively enhances the superharmonic amplitudes along the submerged step. However, the influence is much more significant on the shallower side.

#### D. Skewness and kurtosis

The skewness and kurtosis are parameters that can be used to measure the nonlinearity of the wave profiles. In particular, the skewness measures the level of asymmetry (horizontal) of wave elevation; and the kurtosis measures the growth of the elevation peak or the sharpness—both reflect the influence of nonlinearity. For any Gaussian distribution, the skewness is 0 and the kurtosis is 3 from the properties of a normal distribution. Sea surface elevation kurtosis is often taken as an important indicator of rogue wave activity. Increased kurtosis can indicate an increased probability of the occurrence of suddenly appearing large waves.<sup>14,15</sup> This section discusses the distribution of skewness and kurtosis along the  $x$  axis. Formulas for computing skewness and kurtosis are described in detail in [Appendix D](#).

Although the parameters, skewness, and kurtosis are commonly used in the random statistical distribution, the variation of parameters can indicate the out-of-equilibrium states at the ADT. For a single (monochromatic) linear wave component, the skewness and kurtosis are 0 and 1.5, respectively. The value of kurtosis of regular waves is only half of that of the Gaussian random waves. It can be indeed found that the skewness is about 0.15 and kurtosis is about 1.6 for the incident wave cases. [Figure 18](#) shows the evolution of the skewness and kurtosis for four selected cases in the spatial domain where the shaded area represents the submerged step. It is noticed that both the skewness and kurtosis have grown when the waves propagate through the first ADT, then reach the maxima at the top of the submerged step. The two parameters gradually decrease at the second ADT and return to the incident conditions for several cases. In terms of the skewness, a rise in values is found after the first ADT and an oscillation exists on the shallower region on the step. The oscillation suggests some

distortion of the wave shape on the step. For instance in the case with  $f_0 = 0.94$  Hz and  $k_1 a = 0.06$ , it is found that the maximum point of the skewness is located at nearly  $x = -0.5$  m. Then, a drop of skewness is found after the second ADT, where the value even becomes negative. This phenomenon indicates larger wave troughs are present on the deeper regions and the horizontal surface elevations remain asymmetry. The sudden increase in the skewness clearly shows the horizontal asymmetry of the surface elevation due to the presence of the submerged step. The variation of the skewness is minor for cases with a larger water depth  $h_2/h_1 = 0.52$ .

Similar trends are found for the evolution of kurtosis. The sudden increase in the kurtosis on top of the step suggests that the wave crest is sharpened. This is directly attributed to the increase in the higher harmonics, as demonstrated in [Fig. 14](#). The oscillation may also indicate that the second free waves on the step evolve at a different speed than that of the fundamental harmonics. Again, the kurtosis remains constant for the relatively deeper water. In summary, the existence of the submerged step clearly changes the wave profiles on the step. The skewness and kurtosis suggest that the abrupt depth transitions make the shape's asymmetry more obvious and the crest sharper, a clear result from nonlinear effects.

#### IV. CONCLUSIONS

The nonlinear wave propagation over a submerged step was investigated experimentally and numerically. We focus on the evolution of higher harmonics when waves pass the abrupt depth transitions. The experiment was carried out in a long wave flume with varying wave frequencies and amplitudes. Two water depths were tested. A high-speed camera was installed to capture the wave passing the first ADT, and no obvious flow separation was observed at the edge of the step, suggesting minor viscous effects. A fully nonlinear potential flow model was developed to solve the nonlinear boundary value problem. A conformal mapping method was employed to deal with the free-surface boundary conditions and the varying bottom boundaries. A mapping function was proposed to realize the



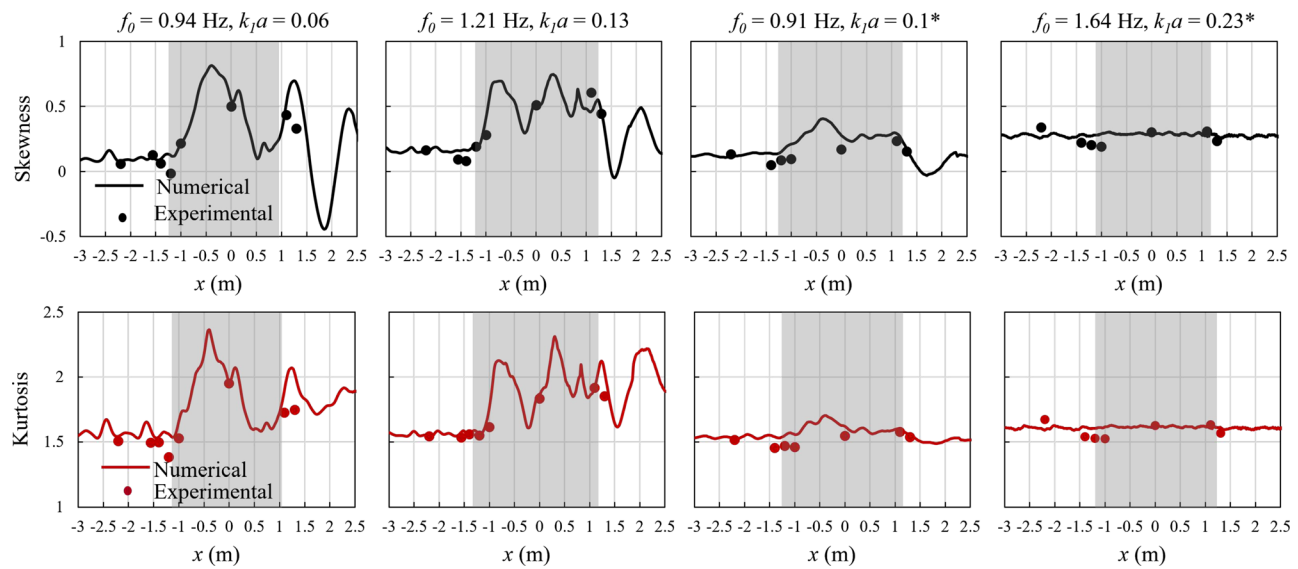


FIG. 18. Spatial evolution of wave skewness and kurtosis in measurements and simulations (\* refers to  $h_2/h_1 = 0.52$ ).

transformation between the physical plane and the mathematical plane. With the aid of nonlinear simulations, it is possible for us to extract the higher harmonics (from second up to fourth) in time and space. With the abrupt depth transitions, direct comparisons of wave surface elevations at all probing locations were made between the simulations and the measurements. The agreement is excellent. The nonlinear model by the conformal mapping method was demonstrated to be suitable for simulating wave propagation over varying bathymetry including the abrupt depth transitions.

We focus on the higher harmonics triggered by the wave interaction with the abrupt depth transitions. The FFT technique is used to extract the higher harmonic components of the wave elevation. A second-harmonic reflection coefficient is defined to show the effect of the presence of the submerged step on the second harmonic waves. It is found that with increasing wave steepness, the nonlinear effect leads to increased second-harmonic reflection coefficients, as expected. Spectral analysis of the time histories of the elevations shows the importance of superharmonics, especially near the middle of the step. For the cases of relatively longer waves with  $h_2/h_1 = 0.36$ , the significant change of water depth at the first ADT clearly makes the wave profile on the step distorted where the wave dispersion plays an important role. The associated higher harmonics also become considerable. With a higher  $h_2/h_1 = 0.52$ , both the dispersion and nonlinear effects become less significant.

The evolution of the separated harmonics along the step is investigated. This is obtained by performing FFT on the time signal of every point on the entire free surface. The sudden increase in the higher harmonics at the first ADT shows the clear interaction of the propagating wave with the submerged step. Some oscillations of the harmonic amplitudes are seen on the step. This might be due to the influence of higher harmonic free waves that can transmit to the downstream side of the step. However, for cases with higher frequency or deeper water depth, the superharmonic components return to the incident amplitudes. It demonstrates that the sudden enhancement of the ADT on

the superharmonic amplitudes may be localized in the shallower regions.

The effects of the incident wave frequency  $k_1 h_1$  and amplitude are studied on the first harmonics and superharmonics (second to fourth). At a lower frequency of the incident wave, we see considerable superharmonic components near the middle of the step (WG 6). Steeper incident waves generally produce larger superharmonics among which the second is the most significant.

The evolution of skewness and kurtosis is computed to evaluate the nonlinear effects at the step. For cases where there is a sudden increase in the skewness over the step, the horizontal asymmetry of the surface elevation can be found as a clear indication of nonlinearity. The similar sudden increase in the kurtosis on top of the step reflects that the wave crest is sharpened due to the increase in the higher harmonics. The asymmetry of the wave profiles and sharpened crest resulting from nonlinear effects may indicate the increase in the possibility of the occurrence of extreme waves at the abrupt depth transitions.

This study demonstrates the capability of a nonlinear numerical model to study the nonlinear wave dynamics on the abrupt depth transitions. Higher harmonic evolution over a submerged step and nonlinear effects of the abrupt depth transitions on higher harmonics are explored. The model can be easily extended to the application of other varying bathymetries and other incident wave types given the feature of the conformal mapping method. The numerical model with the conformal mapping method provides effective prediction methods for the nonlinear evolution of wave profiles and more accurate inputs for the physical problem of the wave–bottom interactions. More investigations that incorporating the developed model into a multiple wave gauges assessment should be conducted in future studies.

## ACKNOWLEDGMENTS

The authors are grateful to Wooyoung Choi and Denys Dudykh for their invaluable assistance in the conformal mapping

method. Their suggestions help to improve the quality of our numerical simulations. Funding from State Key Laboratory of Coastal and Offshore Engineering, Dalian University of Technology (LP2116), and Natural Science Foundation of Shenzhen Municipality (Shenzhen Natural Science Foundation, JCYJ20210324104606017) is highly acknowledged. Financial support from Centers for Mechanical Engineering Research and Education at MIT and SUSTech is also gratefully acknowledged.

## AUTHOR DECLARATIONS

### Conflict of Interest

The authors have no conflicts to disclose.

### Author Contributions

**Qian Wu:** Data curation (equal); Formal analysis (equal); Investigation (equal); Methodology (equal); Validation (equal); Visualization (equal); Writing – original draft (equal). **Xingya Feng:** Conceptualization (equal); Formal analysis (equal); Funding acquisition (equal); Investigation (equal); Methodology (equal); Project administration (equal); Resources (equal); Supervision (equal); Writing – review & editing (lead). **You Dong:** Resources (equal); Supervision (equal); Writing – review & editing (equal). **Frédéric Dias:** Formal analysis (equal); Investigation (equal); Validation (equal); Writing – review & editing (supporting).

## DATA AVAILABILITY

The data that support the findings of this study are available within the article.

## APPENDIX A: TIME WINDOW FOR SPECTRA ANALYSIS

The experiments were conducted in both conditions with and without a submerged step. Prior to the analysis of harmonics, the incident wave height was obtained from cases without a step in the wave tank. Figure 19 compares the input parameters  $H_{in}$  and the actual wave height  $H_{out}$ . This allows for the use of more precise incident waves generated in the laboratory for subsequent investigations.

To process the spectra analysis, the fast Fourier transform (FFT) is used to deal with the surface elevations in the time domain. The time window of surface elevations needs to be selected

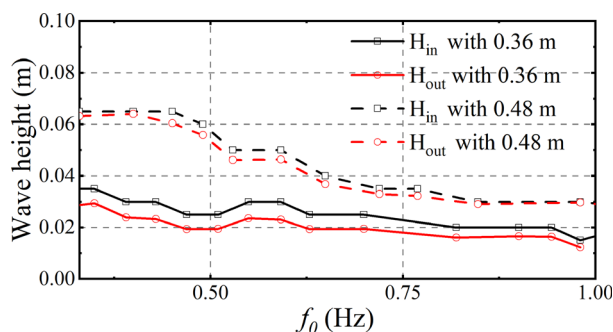


FIG. 19. Wave heights with input parameters and physical outputs.

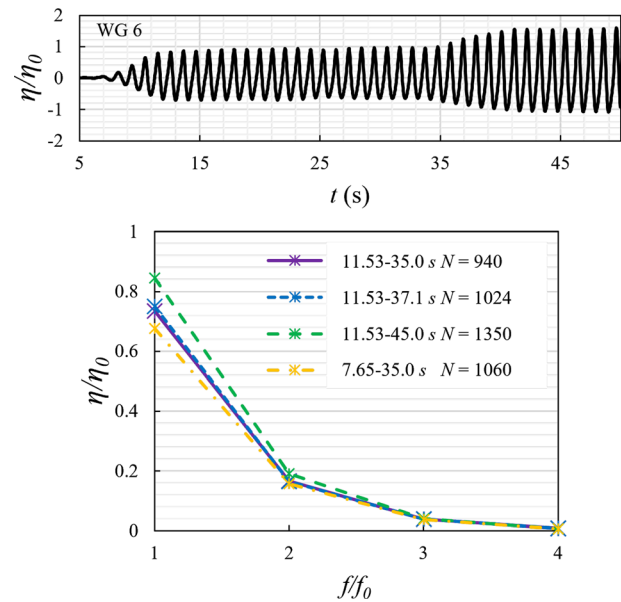


FIG. 20. Selections of surface elevations and harmonic amplitudes for case 1 at WG 6.

appropriately. It should avoid the startup of incident waves before the arrival of steady regular waves and the reflected waves coming from the back of the wave tank. We consider case 1 to examine the results of FFT with different ranges of the time window at WG 6 (Fig. 20). It is found that both the unsteady incident waves and the reflected wave from the backside of the wave tank can affect the amplitude spectra. Meanwhile, there is little difference between the results with the total Fourier discrete points  $n = 940$  and that with  $n = 1024$ .

To extract the superharmonics in the wave signal, the surface elevations must be transformed into the frequency domain by FFT. Then, the range of a certain order harmonics is selected, and the surface elevations are transformed back in the time domain by the IFFT. The higher harmonic frequency is written as

$$f_m = m \cdot f_0, \quad (\text{A1})$$

where  $m = 1, 2, 3, \dots$  represents the order of harmonic waves. To indicate the wave nonlinearity triggered by the ADT, the time for the separated waves in the spatial domain is chosen where 3–4 wave periods have passed the ADT.

## APPENDIX B: SEPARATION OF THE INCIDENT AND REFLECTED WAVES

The computation of the reflection coefficients is based on the analytical method.<sup>47</sup> This is not limited by the phase difference, and two wave gauges  $\eta(x_1, t)$  and  $\eta(x_2, t)$  are enough to process the calculation. For regular waves, the incident and reflected waves are assumed to be

$$\eta_I = A_I \cos(\omega t - kx + \theta_I), \quad (\text{B1})$$

$$\eta_R = A_R \cos(\omega t - kx + \theta_R), \quad (\text{B2})$$

where  $A_I$  and  $A_R$  are the amplitude of the incident and reflected waves, respectively.  $\theta_I$  and  $\theta_R$  refer to the phase angles.  $\omega$  is the angular frequency and  $k$  the wave number. Due to the linear superposition of surface elevations,  $\eta(x_1, t)$  and  $\eta(x_2, t)$  are expressed as

$$\eta(x_1, t) = A_I \cos(\omega t - kx_1 + \theta_I) + A_R \cos(\omega t + kx_1 + \theta_R), \quad (\text{B3})$$

$$\begin{aligned} \eta(x_2, t) &= A_I \cos(\omega t - kx_2 + \theta_I) + A_R \cos(\omega t + kx_2 + \theta_R) \\ &= A_I \cos(\omega t - kx_1 + \theta_I - k\Delta x) \\ &\quad + A_R \cos(\omega t + kx_1 + \theta_R + k\Delta x). \end{aligned} \quad (\text{B4})$$

Let  $x_2 = x_1 + \Delta x$ , so that Eqs. (B3) and (B4) can be reduced to the equation with  $x_1$ . In addition, they can be written in the complex form as

$$\eta(x_1, t) = A_I e^{i(\omega t - kx_1 + \theta_I)} + A_R e^{i(\omega t + kx_1 + \theta_R)}, \quad (\text{B5})$$

$$\eta(x_2, t) = A_I e^{i(\omega t - kx_1 + \theta_I)} e^{-ik\Delta x} + A_R e^{i(\omega t + kx_1 + \theta_R)} e^{ik\Delta x}. \quad (\text{B6})$$

From Eqs. (B5) and (B6), we obtain the surface elevation of the incident and reflected waves,

$$\eta_I(x, t) = A_I e^{i(\omega t - kx_1 + \theta_I)} = \frac{e^{ik\Delta x} \eta(x_1, t) - \eta(x_2, t)}{2i \sin(k\Delta x)}, \quad (\text{B7})$$

$$\eta_R(x, t) = A_R e^{i(\omega t + kx_1 + \theta_R)} = \frac{e^{-ik\Delta x} \eta(x_1, t) - \eta(x_2, t)}{-2i \sin(k\Delta x)}, \quad (\text{B8})$$

$$K_r = \frac{A_R}{A_I} = \frac{|e^{-ik\Delta x} \eta(x_1, t) - \eta(x_2, t)|}{|e^{ik\Delta x} \eta(x_1, t) - \eta(x_2, t)|}. \quad (\text{B9})$$

It should be noticed that the surface elevations recorded at the positions  $x_1$  and  $x_2$  need to be transformed into the complex form by taking a Hilbert transform. The reflection coefficients of the higher harmonic waves can also be computed similarly as long as the input surface elevations  $\eta(x_1, t)$  and  $\eta(x_2, t)$  are replaced by  $\eta_m(x_1, t)$  and  $\eta_m(x_2, t)$  where  $m$  denotes the order of the superharmonics. Note that the higher harmonic reflection coefficients are defined by the ratio of the harmonic amplitudes to the nonlinear wave amplitude. Extraction of the harmonics can be realized by the FFT technique, and the reflection coefficients of the harmonics can be written as

$$K_{rm} = \frac{A_{Rm}}{A_I} = \frac{|e^{-ik_m \Delta x} \eta_m(x_1, t) - \eta_m(x_2, t)|}{|e^{ik_m \Delta x} \eta_m(x_1, t) - \eta_m(x_2, t)|}. \quad (\text{B10})$$

## APPENDIX C: SEPARATION OF SECOND BOUND AND FREE WAVES

The frequency of the second bound waves (lock-in waves  $f_B$ ) is twice that of the incident waves  $f_0$ . However, there is also a free wave  $f_F$  that occurs during wave propagation over varying water depths. The component of free waves obeys the dispersion relation, resulting in a small discrepancy in frequency compared to the bound waves ( $f_B \neq f_F$ ). Additionally, the velocity of free waves differs from that of the bound waves. A common approach to separate these two components is to allow wave propagation with sufficient time and space, such as in the propagation of wave packets. This

method is not applicable in the case of monochromatic waves due to the continuous incident waves. Consequently, a separation technique based on surface elevations at four different wave gauges is adopted.<sup>48</sup> The surface elevations  $\eta(x, t)$  at each position can be expressed as

$$\begin{aligned} \eta(x_p, t) &= A_I^1 (\cos kx_p - \omega t + \phi_I^1) + A_R^1 (\cos kx_p + \omega t + \phi_R^1) \\ &\quad + \sum_{m \geq 2} A_{I,B}^m \cos [m(kx_p - \omega t) + \phi_{I,B}^m] \\ &\quad + \sum_{m \geq 2} A_{R,B}^m \cos [m(kx_p + \omega t) + \phi_{R,B}^m] \\ &\quad + \sum_{m \geq 2} A_{I,F}^m \cos [m(kx_p - \omega t) + \phi_{I,F}^m] \\ &\quad + \sum_{m \geq 2} A_{R,F}^m \cos [m(kx_p + \omega t) + \phi_{R,F}^m] + e_p(t), \end{aligned} \quad (\text{C1})$$

where the subscripts  $B$  and  $F$  denote the bound and free wave components, respectively.  $x_p$  represents the location in the spatial domain. The subscript  $m$  ( $m = 1, 2, \dots$ ) refers to the  $m$ th-order harmonic waves.  $\phi^m$  denotes the phase difference in an arbitrary time domain. The final  $e_p(t)$  is associated with the extra signal noise resulting from nonlinear wave interactions. Then, the surface elevations  $\eta(x_p, t)$  can be decomposed with FFT as

$$\tilde{\eta}^m(x_p) = \frac{\omega}{2\pi} \int_0^{(2\pi/\omega)} \eta(x_p, t) e^{-im\omega t} dt. \quad (\text{C2})$$

By substituting Eq. (C1) into Eq. (C2) and assume  $m = 1$ , the transformed surface elevations can be written as

$$\tilde{\eta}^1(x_p) = C_I^1 X_I^1 + C_R^1 X_R^1 + T_p^1, \quad (\text{C3})$$

where

$$\begin{aligned} X_I^1 &= A_I^1 e^{-i(kx_1 + \phi_I^1)}, \quad X_R^1 = A_R^1 e^{-i(kx_1 + \phi_R^1)}, \\ C_I^1 &= \frac{e^{-ik\Delta x_p}}{2}, \quad C_R^1 = \frac{e^{ik\Delta x_p}}{2}. \end{aligned}$$

The fast Fourier transform of  $e_m(t)$  at  $m = 1$  and the position of wave gauge  $x_1$  is displayed as  $T_p^1$ .  $\Delta x_p$  denotes the distance between the first wave gauge and the  $m$ th wave gauge. The sum of  $T_p^1$  can be minimized using the least squares method to choose the parameters  $X_I^1$  and  $X_R^1$ , namely, the minimum sum

$$\sum_p [T_p^1]^2 = \sum_p [\tilde{\eta}^1(x_p) - C_I^1 X_I^1 - C_R^1 X_R^1]^2. \quad (\text{C4})$$

The solution of parameters  $X_I^1$  and  $X_R^1$  can be obtained by minimizing their total errors,

$$\frac{\partial \sum_p [T_p^1]^2}{\partial X_I^1} = 0, \quad \frac{\partial \sum_p [T_p^1]^2}{\partial X_R^1} = 0, \quad (\text{C5})$$

where the algebraic equations can be simplified as

$$\begin{bmatrix} A_{11} & A_{12} \\ A_{21} & A_{22} \end{bmatrix} \begin{bmatrix} X_I^1 \\ X_R^1 \end{bmatrix} = \begin{bmatrix} B_1 \\ B_2 \end{bmatrix}. \quad (\text{C6})$$

The study by Lin and Huang provides the solution for components  $A_{ij}$  and  $B_i$ . The amplitudes of the first harmonics can be determined as follows:

$$A_I^1 = |X_I^1|, \quad A_R^1 = |X_R^1|. \quad (C7)$$

Similarly, the singularity should be avoided in the physical application. For four different wave gauges before the first depth transition, Eq. (C8) is determined as follows:

$$\left[ \frac{1}{4} + \frac{e^{-2ik\Delta x_2}}{4} + \frac{e^{-2ik\Delta x_3}}{4} \frac{e^{-2ik\Delta x_4}}{4} \right] \times \left[ \frac{1}{4} + \frac{e^{2ik\Delta x_2}}{4} + \frac{e^{2ik\Delta x_3}}{4} \frac{e^{2ik\Delta x_4}}{4} \right] - 1 = O. \quad (C8)$$

To achieve the amplitude of the first harmonics, the same steps are employed for the superharmonic waves by substituting Eq. (C1) into Eq. (C2) with  $m \geq 2$ . Consequently, the transformation of  $\eta(x_p, t)$  is modified to

$$\tilde{\eta}^m(x_p) = C_{I,B}^m X_{I,B}^m + C_{R,B}^m X_{R,B}^m + C_{I,F}^m X_{I,F}^m + C_{R,F}^m X_{R,F}^m + T_p^m, \quad (C9)$$

$$A_{I,B}^m = |X_{I,B}^m|, \quad A_{R,B}^m = |X_{R,B}^m|, \quad A_{I,F}^m = |X_{I,F}^m|, \quad A_{R,F}^m = |X_{R,F}^m|. \quad (C10)$$

#### APPENDIX D: STATISTICAL DISTRIBUTION OF SURFACE ELEVATIONS

The parameters skewness and kurtosis can be useful to describe the statistical distribution of the surface elevation and wave heights. In terms of the surface elevation  $\eta$ , the definitions of skewness and kurtosis are

$$\lambda_3 = \langle (\eta - \langle \eta \rangle)^3 \rangle / \eta_{std}^3, \quad \lambda_4 = \langle (\eta - \langle \eta \rangle)^4 \rangle / \eta_{std}^4, \quad (D2)$$

where  $\eta_{std}$  is the standard deviation of the surface elevation. The values are  $\lambda_3 = 0$  and  $\lambda_4 = 3$  for Gaussian waves. There is a clear increase in the values on the shallower regions, inducing a higher probability of occurrence of extreme waves on the abrupt depth transitions.

#### REFERENCES

- I. Didenkulova, A. Slunyaev, E. Pelinovsky, and C. Kharif, "Freak waves in 2005," *Nat. Hazards Earth Syst. Sci.* **6**, 1007–1015 (2006).
- E. Didenkulova and E. Pelinovsky, "Freak waves in 2011–2018," in *Doklady Earth Sciences* (Springer, 2020), Vol. 491, pp. 187–190.
- I. Nikolkina and I. Didenkulova, "Rogue waves in 2006–2010," *Nat. Hazards Earth Syst. Sci.* **11**, 2913–2924 (2011).
- I. Teutsch, R. Weisse, J. Moeller, and O. Krueger, "A statistical analysis of rogue waves in the southern north sea," *Nat. Hazards Earth Syst. Sci.* **20**, 2665–2680 (2020).
- Y. P. Sheng, Y. Zhang, and V. A. Paramygin, "Simulation of storm surge, wave, and coastal inundation in the Northeastern Gulf of Mexico region during Hurricane Ivan in 2004," *Ocean Modell.* **35**, 314–331 (2010).
- M. Onorato, S. Residori, U. Bortolozzo, A. Montina, and F. Arecchi, "Rogue waves and their generating mechanisms in different physical contexts," *Phys. Rep.* **528**, 47–89 (2013).
- J. M. Dudley, G. Genty, A. Mussot, A. Chabchoub, and F. Dias, "Rogue waves and analogies in optics and oceanography," *Nat. Rev. Phys.* **1**, 675–689 (2019).
- J. D. Hansom, A. D. Switzer, and J. Pile, "Extreme waves: Causes, characteristics, and impact on coastal environments and society," in *Coastal and Marine Hazards, Risks, and Disasters* (Elsevier, 2015) pp. 307–334.
- F. Copie, S. Randoux, and P. Suret, "The physics of the one-dimensional nonlinear Schrödinger equation in fiber optics: Rogue waves, modulation instability and self-focusing phenomena," *Rev. Phys.* **5**, 100037 (2020).
- S.-H. Ou, J.-M. Liao, T.-W. Hsu, and S.-Y. Tzang, "Simulating typhoon waves by SWAN wave model in coastal waters of Taiwan," *Ocean Eng.* **29**, 947–971 (2002).
- S. Mendes, A. Scotti, M. Brunetti, and J. Kasparian, "Non-homogeneous analysis of rogue wave probability evolution over a shoal," *J. Fluid Mech.* **939**, A25 (2022).
- H. Chien, C.-C. Kao, and L. Z. Chuang, "On the characteristics of observed coastal freak waves," *Coastal Eng. J.* **44**, 301–319 (2002).
- Y. Li, Y. Zheng, Z. Lin, T. A. Adcock, and T. S. van den Bremer, "Surface wave-packets subject to an abrupt depth change—Part 1: Second-order theory," *J. Fluid Mech.* **915**, A71 (2021).
- K. Trulsen, A. Raustøl, S. Jorde, and L. B. Rye, "Extreme wave statistics of long-crested irregular waves over a shoal," *J. Fluid Mech.* **882**, R2 (2020).
- J. Zhang and M. Benoit, "Wave-bottom interaction and extreme wave statistics due to shoaling and de-shoaling of irregular long-crested wave trains over steep seabed changes," *J. Fluid Mech.* **912**, A28 (2021).
- M. S. Afzal and L. Kumar, "Propagation of waves over a rugged topography," *J. Ocean Eng. Sci.* **7**, 14–28 (2022).
- J. Zhang, M. Benoit, O. Kimmoun, A. Chabchoub, and H.-C. Hsu, "Statistics of extreme waves in coastal waters: Large scale experiments and advanced numerical simulations," *Fluids* **4**, 99 (2019).
- C. T. Bolles, K. Speer, and M. Moore, "Anomalous wave statistics induced by abrupt depth change," *Phys. Rev. Fluids* **4**, 011801 (2019).
- A. J. Majda, M. Moore, and D. Qi, "Statistical dynamical model to predict extreme events and anomalous features in shallow water waves with abrupt depth change," *Proc. Natl. Acad. Sci.* **116**, 3982–3987 (2019).
- M. A. Chella, H. Bihs, D. Myrhaug, and M. Muskulus, "Breaking characteristics and geometric properties of spilling breakers over slopes," *Coastal Eng.* **95**, 4–19 (2015).
- Y. Zheng, Z. Lin, Y. Li, T. Adcock, Y. Li, and T. Van Den Bremer, "Fully nonlinear simulations of unidirectional extreme waves provoked by strong depth transitions: The effect of slope," *Phys. Rev. Fluids* **5**, 064804 (2020).
- M.-S. Li, C.-J. Hsu, H.-C. Hsu, and L.-H. Tsai, "Numerical analysis of vertical breakwater stability under extreme waves," *J. Mar. Sci. Eng.* **8**, 986 (2020).
- H.-K. Chang and J.-C. Liou, "Long wave reflection from submerged trapezoidal breakwaters," *Ocean Eng.* **34**, 185–191 (2007).
- Q. Ji, S. Dong, X. Luo, and C. G. Soares, "Wave transformation over submerged breakwaters by the constrained interpolation profile method," *Ocean Eng.* **136**, 294–303 (2017).
- D. G. Stamos, M. R. Hajj, and D. P. Telonis, "Performance of hemi-cylindrical and rectangular submerged breakwaters," *Ocean Eng.* **30**, 813–828 (2003).
- K. Trulsen, "Rogue waves in the ocean, the role of modulational instability, and abrupt changes of environmental conditions that can provoke non equilibrium wave dynamics," in *The Ocean in Motion* (Springer, 2018) pp. 239–247.
- S. Massel, "Harmonic generation by waves propagating over a submerged step," *Coastal Eng.* **7**, 357–380 (1983).
- C. C. Mei, M. A. Stiassnie, and D. K.-P. Yue, *Theory and Applications of Ocean Surface Waves: Part 1: Linear Aspects* (World Scientific, 2005).
- H.-W. Liu, D.-J. Fu, and X.-L. Sun, "Analytic solution to the modified mild-slope equation for reflection by a rectangular breakwater with scour trenches," *J. Eng. Mech.* **139**, 39–58 (2013).
- L. Gorrell, B. Raubenheimer, S. Elgar, and R. Guza, "Swan predictions of waves observed in shallow water onshore of complex bathymetry," *Coastal Eng.* **58**, 510–516 (2011).
- S. Zhao, J. Zhou, C. Jing, and L. Li, "Improved finite volume method for solving 1-D advection equation," *J. Phys.: Conf. Ser.* **1300**, 012075 (2019).
- J. G. Herterich and F. Dias, "Extreme long waves over a varying bathymetry," *J. Fluid Mech.* **878**, 481–501 (2019).
- C. Lawrence, K. Trulsen, and O. Gramstad, "Extreme wave statistics of surface elevation and velocity field of gravity waves over a two-dimensional bathymetry," *J. Fluid Mech.* **939**, A41 (2022).
- T. Tang and T. A. Adcock, "The influence of finite depth on the evolution of extreme wave statistics in numerical wave tanks," *Coastal Eng.* **166**, 103870 (2021).
- J.-F. Lee, L.-F. Tu, and C.-C. Liu, "Nonlinear wave evolution above rectangular submerged structures," *J. Mar. Sci. Technol.* **22**(5), 531–541 (2014).
- N. J. Moore, C. T. Bolles, A. J. Majda, and D. Qi, "Anomalous waves triggered by abrupt depth changes: Laboratory experiments and truncated kdv statistical mechanics," *J. Nonlinear Sci.* **30**, 3235–3263 (2020).



- <sup>37</sup>Y. Li, S. Draycott, Y. Zheng, Z. Lin, T. A. Adcock, and T. S. van den Bremer, "Why rogue waves occur atop abrupt depth transitions," *J. Fluid Mech.* **919**, R5 (2021).
- <sup>38</sup>S. Draycott, Y. Li, P. Stansby, T. Adcock, and T. van den Bremer, "Harmonic-induced wave breaking due to abrupt depth transitions: An experimental and numerical study," *Coastal Eng.* **171**, 104041 (2022).
- <sup>39</sup>J. Zhang, M. Benoit, and Y. Ma, "Equilibration process of out-of-equilibrium sea-states induced by strong depth variation: Evolution of coastal wave spectrum and representative parameters," *Coastal Eng.* **174**, 104099 (2022).
- <sup>40</sup>A. Galan, G. Simarro, A. Orfila, J. Simarro, and P.-F. Liu, "Fully nonlinear model for water wave propagation from deep to shallow waters," *J. Waterway, Port, Coastal, Ocean Eng.* **138**, 362–371 (2012).
- <sup>41</sup>K. Trulsen, H. Zeng, and O. Gramstad, "Laboratory evidence of freak waves provoked by non-uniform bathymetry," *Phys. Fluids* **24**, 097101 (2012).
- <sup>42</sup>C. Viotti, D. Dutykh, and F. Dias, "The conformal-mapping method for surface gravity waves in the presence of variable bathymetry and mean current," *Proc. IUTAM* **11**, 110–118 (2014).
- <sup>43</sup>A. I. Dyachenko, E. A. Kuznetsov, M. Spector, and V. E. Zakharov, "Analytical description of the free surface dynamics of an ideal fluid (canonical formalism and conformal mapping)," *Phys. Lett. A* **221**, 73–79 (1996).
- <sup>44</sup>W. Choi and R. Camassa, "Exact evolution equations for surface waves," *J. Eng. Mech.* **125**, 756–760 (1999).
- <sup>45</sup>C. Lawrence, O. Gramstad, and K. Trulsen, "Variational Boussinesq model for kinematics calculation of surface gravity waves over bathymetry," *Wave Motion* **100**, 102665 (2021).
- <sup>46</sup>C. Viotti and F. Dias, "Extreme waves induced by strong depth transitions: Fully nonlinear results," *Phys. Fluids* **26**, 051705 (2014).
- <sup>47</sup>Y. Wang, J. Peng, H. Sun, and G. Li, "Separation of composite waves by an analytical method," *Ocean Eng.* **21**(1), 42–46 (2003).
- <sup>48</sup>C.-Y. Lin and C.-J. Huang, "Decomposition of incident and reflected higher harmonic waves using four wave gauges," *Coastal Eng.* **51**, 395–406 (2004).
- <sup>49</sup>M. Loukili, D. Dutykh, S. Pincemin, K. Kotrasova, and N. Abcha, "Theoretical investigation applied to scattering water waves by rectangular submerged obstacles/and submarine trenches," *Geosciences* **12**, 379 (2022).
- <sup>50</sup>J. Peng, A. Tao, J. Fan, J. Zheng, and Y. Liu, "On the downshift of wave frequency for Bragg resonance," *China Ocean Eng.* **36**, 76–85 (2022).
- <sup>51</sup>T. L. Andersen, M. R. Eldrup, and P. Frigaard, "Estimation of incident and reflected components in highly nonlinear regular waves," *Coastal Eng.* **119**, 51–64 (2017).
- <sup>52</sup>C. Mei and U. Unluata, "Harmonic generation in shallow water waves," in *Waves on Beaches and Resulting Sediment Transport* (Elsevier, 1972), pp. 181–202.
- <sup>53</sup>A. Kurkin, S. Semin, and Y. A. Stepanyants, "Transformation of surface waves over a bottom step," *Izv., Atmos. Oceanic Phys.* **51**, 214–223 (2015).
- <sup>54</sup>A. Giniyatullin, A. Kurkin, S. Semin, and Y. A. Stepanyants, "Transformation of narrowband wavetrains of surface gravity waves passing over a bottom step," *Math. Modell. Nat. Phenom.* **9**, 73–82 (2014).
- <sup>55</sup>M. Christou, C. Swan, and O. Gudmestad, "The interaction of surface water waves with submerged breakwaters," *Coastal Eng.* **55**, 945–958 (2008).